

GEORCE: A Fast New Control Algorithm for Computing Geodesics

Frederik Möbius Rygaard^{1*} and Søren Hauberg^{1*}

^{1*}DTU Compute, Technical University of Denmark (DTU), Anker Engelundsvej 1, Kongens Lyngby, 2800, Denmark.

*Corresponding author(s). E-mail(s): fmry@dtu.dk; sohau@dtu.dk;

Abstract

Computing geodesics for Riemannian manifolds is a difficult task that often relies on numerical approximations. However, these approximations tend to be either numerically unstable, have slow convergence, or scale poorly with manifold dimension and number of grid points. We introduce a new algorithm called *GEORCE* that computes geodesics via a transformation into a discrete control problem. We show that *GEORCE* has global convergence and quadratic local convergence. In addition, we show that it extends to Finsler manifolds. For both Finslerian and Riemannian manifolds, we thoroughly benchmark *GEORCE* against several alternative optimization algorithms and show empirically that it has a much faster and more accurate performance for a variety of manifolds, including key manifolds from information theory and manifolds that are learned using generative models.

Keywords: Riemannian Manifolds, Finsler Manifolds, Geodesics, Optimization, Control Problem

Mathematics Subject Classification 53C22, 49Q99, 65D15

1 Introduction

Reliably computing geodesics that connect point pairs is a constant source of frustration to practitioners working with non-trivial Riemannian manifolds. Such manifolds see common use across many fields, including medical image analysis [1–3], protein modeling [4–6], robotics [7–10], generative modeling [11–16] and information geometry [17–21].

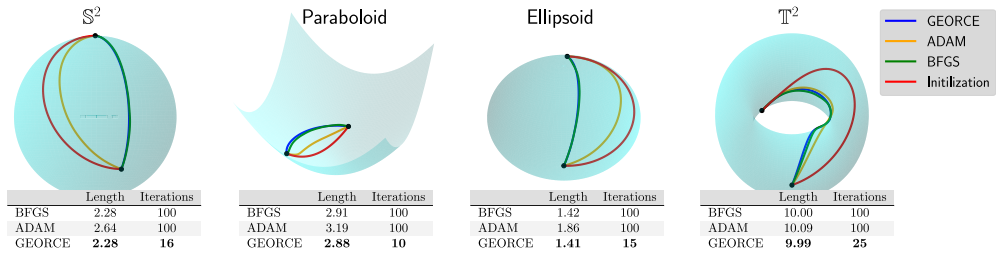


Fig. 1 Comparison between *GEORCE* and baseline methods for computing locally length minimizing geodesics between given point pairs on four different manifolds. All algorithms are terminated if the ℓ^2 -norm of the gradient of the discretized energy functional (5) is less than 10^{-4} , or the number of iterations exceeds 100. Note that sometimes the respective solutions overlap, making it difficult to distinguish them. Also note, that in the case of the torus the initial curve determines the direction around the hole so that the obtained geodesics follow this direction and are therefore clearly not the globally shortest geodesics between the given start and end point. Experimental details and benchmark data are in Appendix E.

Geodesics, or *locally shortest paths*, are the key computational tools for engaging with data residing on a Riemannian manifold. The lengths of geodesic curves inform us about manifold distances. Likewise, the *exponential* and *logarithm maps*, which generalize addition and subtraction, are rooted in geodesics [22]. Unfortunately, the solution to the boundary-value problem for geodesics are only available in closed form for the simplest manifolds, and numerical approximations are therefore required in practice.

Such approximations are typically achieved by minimizing the *energy functional* over a suitable set of curves connecting the given boundary points and parametrized by $\gamma : [0, 1] \rightarrow \mathcal{M}$ [23]

$$\mathcal{E}(\gamma) = \frac{1}{2} \int_0^1 \dot{\gamma}(t)^\top G(\gamma(t)) \dot{\gamma}(t) dt, \quad (1)$$

where G denotes the metric matrix function of the manifold in local coordinates. This energy is commonly minimized with general-purpose gradient-based optimization methods [12, 24, 25] or, in particular when considering the initial value problem and using shooting methods, by solving the system of ordinary differential equations that arise by applying the Euler-Lagrange equations [26, 27]. Unfortunately, both approaches are often numerically brittle, exhibit slow convergence, or scale poorly with the number of grid points and manifold dimensions.

In this paper, we introduce the *GEORCE* algorithm (*GEodesic Optimization algoRithm using Control tEchniques*) that computes numerical solutions to the geodesic boundary value problem via an optimal control strategy. *GEORCE* applies to general Riemannian as well as general Finslerian manifolds. We show that the algorithm has global convergence similar to gradient descent and that it has quadratic local convergence similar to the Newton method. Empirically, we compare *GEORCE* with alternative optimization algorithms on the discretized energy functional and see that *GEORCE* is much faster and attains lower Riemannian length as illustrated in Fig. 1.

2 Background and related work

A **Riemannian manifold**, (\mathcal{M}, g) , can indirectly be considered as a smooth n -dimensional surface in a Euclidean space of sufficiently high dimension, see [28, 29]. In this way \mathcal{M} inherits its metric g from the ambient space. All the intrinsic geometry of (\mathcal{M}, g) , including curvature and geodesic distances, are encoded in the metric g . The metric can be – and often is – constructed independently of the formal embedding alluded to above, namely directly as a symmetric positive definite matrix valued function on the domain of a parametrization of the manifold in question. The metric, $g : T_x\mathcal{M} \times T_x\mathcal{M} \rightarrow \mathbb{R}$, defines an inner product that smoothly varies over the tangent spaces of \mathcal{M} such that in a local chart $g(v, w) = v^\top G(x)w$, where G is the metric matrix function evaluated in $x \in \mathcal{M}$ for $v, w \in T_x\mathcal{M}$. The tangent space, $T_x\mathcal{M}$, consists of tangents to all curves at $x \in \mathcal{M}$ [23].

A **geodesic** can then be defined using the inner product in each tangent space. The length of a curve, $\gamma : U \subseteq [0, 1] \rightarrow \mathcal{M}$ parameterized by $t \in [0, 1]$ is given by

$$\mathcal{L}(\gamma) = \int_0^1 \sqrt{\dot{\gamma}(t)^\top G(\gamma(t))\dot{\gamma}(t)} dt, \quad (2)$$

with the corresponding energy given by eq. 1. A geodesic is a smooth curve that locally minimizes the length between two points $x, y \in \mathcal{M}$ and gives rise to the Riemannian distance, $\text{dist} : \mathcal{M} \times \mathcal{M} \rightarrow \mathbb{R}_+$, which is defined as the length of the corresponding shortest geodesic between the given two points on the manifold [23]. It can be shown that if a curve γ locally minimizes the energy (1), then the curve has constant velocity and locally minimizes the length [30]. For general Riemannian manifolds, existence and uniqueness are only guaranteed in a star-shaped neighborhood around any point $x \in \mathcal{M}$ [23]. All points, where the geodesics from a point $x \in \mathcal{M}$ are no longer length minimizing, are denoted the cut locus of x [23]. In this paper, we assume that the manifold is geodesically complete such that at least one length-minimizing geodesic exists between any two points $x, y \in \mathcal{M}$.

A Riemannian manifold can be equipped with a unique metrically compatible connection, ∇ , known as the Levi-Civita Connection [23], where uniqueness and existence are guaranteed by completeness of the metric [23]. An equivalent way to define geodesics is to define these as curves, γ , with zero acceleration using the Levi-Civita connection as the covariant derivative, i.e., $\nabla_{\dot{\gamma}(t)}\dot{\gamma}(t) = 0$. In a local chart, this gives rise to the following (usually non-linear) ODE-system [23]

$$\frac{d^2\gamma^k}{dt^2} + \Gamma_{ij}^k \frac{d\gamma^i}{dt} \frac{d\gamma^j}{dt} = 0, \quad \gamma(0) = a, \gamma(1) = b, \quad (3)$$

written in Einstein notation¹, where $\{\Gamma_{ij}^k\}_{i,j,k}$ denote the Christoffel symbols. The exponential map $\text{Exp}_x(v) : T_x\mathcal{M} \rightarrow \mathcal{M}$ is then defined as $\text{Exp}_x(v) = \gamma(1)$, where γ is a geodesic with $\gamma(0) = x \in \mathcal{M}$ and initial velocity vector, $v \in T_x\mathcal{M}$, i.e. $\dot{\gamma}(0) = v$.

¹In Einstein notation, upper and lower indices constitute a sum, i.e. $a^i b_i = \sum_i a_i b_i$

Within the cut locus of $x \in \mathcal{M}$ the exponential map, Exp_x , is a diffeomorphism and its inverse is the logarithmic map, $\text{Log}_x : \mathcal{M} \rightarrow T_x\mathcal{M}$.

Examples of Riemannian manifolds include information geometric spaces, i.e., statistical manifolds, where “points” in the manifold correspond to statistical distributions. These can be equipped with the so-called Fisher-Rao metric, see [18, 31]:

$$G_{ij}(\theta) = \int_{\mathcal{X}} p(x|\theta) \left(\frac{\partial}{\partial \theta^i} \log p(x|\theta) \right) \left(\frac{\partial}{\partial \theta^j} \log p(x|\theta) \right) d\mu(x), \quad (4)$$

where θ corresponds to the parameters of the probability density function p under a measure μ . Informally, the Fisher-Rao metric can be seen as a measure of the amount of information in the data around a parameter θ [32].

The energy functional in eq. 1 can be discretized and minimized using standard optimization methods. Consider fixed start and end points $x_0 = a \in \mathcal{M}$ and $x_T = b \in \mathcal{M}$, and let $x_{0:T} := \{x_t\}_{t=0}^T$ denote a discretized version of the candidate curve γ in $T + 1$ points. Minimizing the energy functional can be re-written as a discrete constrained optimization problem, i.e., subdivision of $[0, 1]$ into T subintervals, in the chosen local coordinate system [12, 25]

$$E(x_{0:T}) = \min_{x_{0:T}} \sum_{t=0}^{T-1} (x_{t+1} - x_t)^\top G(x_t) (x_{t+1} - x_t) \quad (5)$$

s.t. $x_0 = a, x_T = b,$

where $G(\cdot)$ denotes the metric matrix function in local coordinates, and the tangent vectors of the coordinate expression for γ are discretized as $\dot{\gamma}(t) \approx (x_{t+1} - x_t) T$. Note that the constant scaling by $1/2$ is omitted since it does not affect the optimal solution. With this formulation, the curve is approximated as a piece-wise linear function. This is not restrictive since γ can be approximated into a curve for any given precision T or converted to a smooth function, e.g., using splines [24].

The optimization problem in eq. 5 can be solved using standard solvers in the variables $x_{1:(T-1)}$. Gradient descent converges to a local minimum (*global convergence*), but will have local linear convergence, while a Newton method or quasi-Newton method will have local quadratic and super-linear convergence, respectively, but will involve solving a linear equation system and will, in general, not have global convergence [33].

Limitations of existing numerical solvers. Solving the ODE-system in eq. 3 as a boundary value problem (BVP) can have difficulties converging depending on the choice of initial velocity vector [26] and does not scale well in higher dimension. We illustrate this in Fig. 2, where we show the estimated length and runtime for \mathbb{S}^n with $n = 2, 3, 5, 10, 20$ for different integration methods compared to our proposed algorithm (*GEORCE*). Different approaches try to circumvent this by solving the BVP on subintervals [26, 34] or solving the BVP-problem as a fixed-point problem in a probabilistic manner [35, 36]. However, these methods often require access to higher-order information about the metric tensor, e.g in the form of Christoffel symbols.

Directly minimizing the energy in Eq. 5 can, e.g., be done using off-the-self solvers like *ADAM* [41] or *BFGS* [37–40]. However, these methods tend to have slow convergence and scale poorly in the manifold dimension and number of grid points (see Sec. 5). Alternatively, the geodesic can be estimated by discretizing the smooth manifold by simplicial complexes [42], for which there exist different geodesic solvers [43–47]. Although discretized manifolds appear naturally in computational geometry, the approach is not scalable to discretize high-dimensional smooth manifolds.

3 GEORCE

To develop an efficient primal-dual algorithm for computing geodesics, we will first reformulate the discretized energy functional (5) as a discrete control problem. We then derive the necessary conditions for a minimum for the control problem using techniques from optimal control to decompose the discrete control problem into strictly convex subproblems; from this, we deduce an iterative scheme to compute geodesics. Finally, we prove that our proposed algorithm exhibits global convergence and local quadratic convergence.

As a starting point, we reformulate the problem of finding a minimum of the discrete energy functional (5) to a control problem

$$\begin{aligned} \min_{(x_{1:T-1}, u_{0:T-1})} \quad & \left\{ \sum_{t=0}^{T-1} u_t^\top G(x_t) u_t \right\} \\ \text{s.t.} \quad & x_{t+1} = x_t + u_t, \quad t = 0, \dots, T-1, \\ & x_0 = a, x_T = b. \end{aligned} \tag{6}$$

Here, $x_{0:T}$ denotes the state variables, while $u_{0:(T-1)}$ corresponds to the control variables, i.e., the velocity vectors along the curve (modulo scaling). A key insight into our approach is that rephrasing into an optimal control problem leads to a set of convex subproblems. Using this, we derive the following proposition.

Proposition 1 *The necessary conditions for a minimum in Eq. 6 is*

$$\begin{aligned} 2G(x_t)u_t + \mu_t &= 0, \quad t = 0, \dots, T-1, \\ x_{t+1} &= x_t + u_t, \quad t = 0, \dots, T-1, \\ \nabla_y \left[u_t^\top G(y) u_t \right] \Big|_{y=x_t} + \mu_t &= \mu_{t-1}, \quad t = 1, \dots, T-1. \\ x_0 &= a, x_T = b, \end{aligned} \tag{7}$$

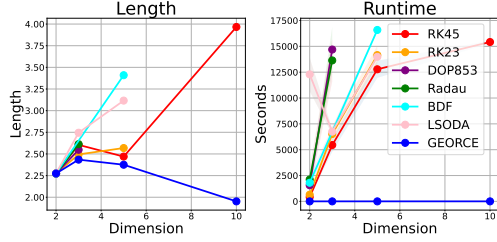


Fig. 2 The estimates of BVP-solvers with different integration methods compared to *GEORCE* on \mathbb{S}^n for $n = 2, 3, 5, 10$. The BVP-solvers minimize the squared error to the boundary condition using *BFGS* [37–40]. All methods are terminated if they take more than 24 hours or use more than 10 GB of memory on a CPU. Details on the experiment is found in Appendix E.1.

where $\mu_t \in \mathbb{R}^d$ for $t = 0, \dots, T-1$.

Proof See Appendix A.2. □

Proposition 1 decomposes the minimization problem in Eq. 6 into a system of equations for each time step t . Note that these equations are necessary conditions for the optimum for eq. 6 and are sufficient in the case where the objective function in eq. 6 is convex in both x_t and u_t . However, this is generally not the case.

The problem with the necessary conditions in Proposition 1 is that the equations cannot be solved in closed form for a general metric matrix function, G . To circumvent this, we will derive an iterative scheme. Consider the variables $x_{0:T}^{(i)}$ and $u_{0:T}^{(i)}$ in iteration i . We apply the “trick” of fixing the metric matrix function, and the derivative of the inner product in iteration i .

$$\begin{aligned} \nu_t &:= \nabla_y (u_t^\top G(y) u_t) \Big|_{y=x_t^{(i)}, u_t=u_t^{(i)}}, \quad t = 1, \dots, T-1, \\ G_t &:= G(x_t^{(i)}), \quad t = 0, \dots, T-1, \end{aligned} \tag{8}$$

Fixing these in iteration i , the system of equations in Eq. 7 reduces to

$$\begin{aligned} 2G_t u_t + \mu_t &= 0, \quad t = 0, \dots, T-1, \\ \nu_t + \mu_t &= \mu_{t-1}, \quad t = 1, \dots, T-1, \\ \sum_{t=0}^{T-1} u_t &= b - a, \end{aligned} \tag{9}$$

where $\nu_{1:(T-1)}$ and $G_{0:(T-1)}$ are fixed (8). Since $G_{0:(T-1)}$ are positive definite, the modified system of equations in Eq. 9 can be explicitly solved in iteration i for $u_{0:(T-1)}$ and $\mu_{0:(T-1)}$ as shown in the following proposition.

Proposition 2 *The update scheme for u_t, μ_t and x_t is*

$$\begin{aligned} \mu_{T-1} &= \left(\sum_{t=0}^{T-1} G_t^{-1} \right)^{-1} \left(2(a-b) - \sum_{t=0}^{T-1} G_t^{-1} \sum_{t>j}^{T-1} \nu_j \right), \\ u_t &= -\frac{1}{2} G_t^{-1} \left(\mu_{T-1} + \sum_{j>t}^{T-1} \nu_j \right), \quad t = 0, \dots, T-1, \\ x_{t+1} &= x_t + u_t, \quad t = 0, \dots, T-1, \\ x_0 &= a. \end{aligned} \tag{10}$$

Proof See Appendix A.3. □

Algorithm 1 GEORCE for Riemannian manifolds

1: **Input:** tol, T
 2: **Output:** Geodesic estimate $x_{0:T}$
 3: Set $x_t^{(0)} \leftarrow a + \frac{b-a}{T}t$, $u_t^{(0)} \leftarrow \frac{b-a}{T}$ for $t = 0, \dots, T$ and $i \leftarrow 0$
 4: **while do** $\left\| \nabla_y E(y) \Big|_{y=x_t^{(i)}} \right\|_2 > \text{tol}$
 5: $G_t \leftarrow G \left(x_t^{(i)} \right)$ for $t = 0, \dots, T-1$
 6: $\nu_t \leftarrow \nabla_y \left(u_t^{(i)} G(y) u_t^{(i)} \right) \Big|_{y=x_t^{(i)}}$ for $t = 1, \dots, T-1$
 7: $\mu_{T-1} \leftarrow \left(\sum_{t=0}^{T-1} G_t^{-1} \right)^{-1} \left(2(a-b) - \sum_{t=0}^{T-1} G_t^{-1} \sum_{t>j}^{T-1} \nu_j \right)$
 8: $u_t \leftarrow -\frac{1}{2} G_t^{-1} \left(\mu_{T-1} + \sum_{j>t}^{T-1} \nu_j \right)$ for $t = 0, \dots, T-1$
 9: $x_{t+1} \leftarrow x_t + u_t$ for $t = 0, \dots, T-1$
 10: Using line search find α^* for the following optimization problem with the discrete energy functional E

$$\alpha^* = \arg \min_{\alpha} E(x_{0:T}) \quad (\text{exact line search})$$

$$\text{s.t. } x_{t+1} = x_t + \alpha u_t + (1-\alpha)u_t^{(i)}, \quad t = 0, \dots, T-1,$$

$$x_0 = a.$$

 11: Set $u_t^{(i+1)} \leftarrow \alpha^* u_t + (1-\alpha^*)u_t^{(i)}$ for $t = 0, \dots, T-1$
 12: Set $x_{t+1}^{(i+1)} \leftarrow x_t^{(i+1)} + u_t^{(i+1)}$ for $t = 0, \dots, T-1$
 13: $i \leftarrow i + 1$
 14: **end while**
 15: return x_t for $t = 0, \dots, T-1$

Proposition 2 immediately leads to an iterative updating of $(x_t^{(i)}, u_t^{(i)})$ to estimate the geodesic, which we denote the *GEORCE*-algorithm. *GEORCE* is described in pseudo-code in Algorithm 1.

Line search and stopping criteria

We find that an appropriate step size is necessary to ensure global convergence for *GEORCE* (See Proposition 3), and therefore we update $u_t^{(i+1)} \leftarrow \alpha u_t^{(i+1)} + (1-\alpha)u_t^{(i)}$ in iteration i . Here, α denotes the step size, which we estimate with line search. One approach is to estimate the optimal step size in each iteration, but, in our experience, this is unnecessarily expensive. We instead use *soft* line search, which merely ensures that the objective function decreases in each iteration [33]. We implement this using backtracking, where an initial step size is multiplied by a decay rate, $0 < \rho < 1$, until some condition is met, e.g., the Wolfe condition [48], the Armijo condition [49], or the curvature condition [48]. In practice, we find that the Armijo condition [49] with $\rho = 0.5$ is sufficient for most manifolds, although the decay rate can be fine-tuned to increase the performance of *GEORCE*.

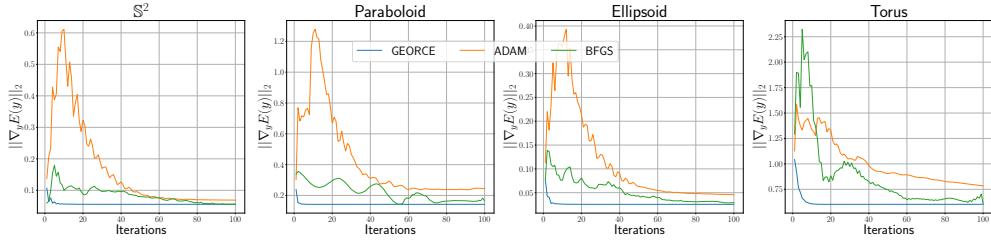


Fig. 3 The figure shows the ℓ^2 -norm of the gradient of eq. 5 for each iteration for *GEORCE* and alternative methods applied to construct geodesics for 100 iterations for four different manifolds corresponding to Fig. 1. We see that the ℓ^2 -norm of the gradient of eq. 5 for *GEORCE* converges considerably faster than for alternative algorithms.

We threshold the ℓ^2 -norm of the gradient of the discrete energy functional as a stopping criteria for *GEORCE*. In all empirical comparisons, identical stopping criteria are applied to all optimization algorithms.

Convergence results

In the following, we show that *GEORCE* is guaranteed to converge to a local minimum, i.e., it exhibits global convergence.

Proposition 3 (Global convergence) *Let $E^{(i)}$ be the value of the discretized energy functional for the solution after iteration i (with line search) in *GEORCE*. If the starting point $(x^{(0)}, u^{(0)})$ is feasible in the sense that the geodesic candidate has the correct start and end points, then the series $\{E^{(i)}\}_{i>0}$ will converge to a (local) minimum.*

Proof See Appendix A.5 for the proof. □

In theory, *GEORCE* could jump between two local minima with the same objective value unless the local minimum is strongly unique, as described in Appendix A.1, and seen in conjugate points [23]. Proposition 3 ensures that *GEORCE* converges to a local minimum (global convergence) similar to gradient descent. In contrast, gradient descent has only linear local convergence, but we show in the following that under sufficient regularity of the discretized energy functional (see Appendix A.1), *GEORCE* has quadratic local convergence.

Proposition 4 (Local quadratic convergence) *Under sufficient regularity of the discretized energy functional (see Appendix A.1) it holds that if the discretized energy functional has a strongly unique (local) minimum point z^* (see Appendix A.1) and locally the step-size $\alpha^* = 1$, i.e., no line search, then *GEORCE* has locally quadratic convergence, i.e.,*

$$\exists \epsilon > 0 : \quad \exists c > 0 : \quad \forall z^{(i)} \in B_\epsilon(z^*) : \quad \left\| z^{(i+1)} - z^* \right\| \leq c \left\| z^{(i)} - z^* \right\|^2,$$

where $z^{(i)} = (x^{(i)}, u^{(i)})$ is the solution from *GEORCE* in iteration i , and $B_\epsilon(z^*)$ is the ball with radius $\epsilon > 0$ and center z^* .

Proof See Appendix A.6 for the proof and Appendix A.1 for the assumptions. \square

Fig. 3 demonstrates the convergence by plotting the ℓ^2 -norm of the gradient of the discretized energy functional in each iteration for four different manifolds. Note that by formulating the geodesic boundary problem as a control problem, we estimate the discretized tangent vectors along the curve $\{u_t\}_{t=0}^T$. Modulo scaling u_0 will in the limit of a sufficiently fine grid correspond to the logarithmic map, $\text{Log}_a b$.

Algorithm	Global convergence	Local convergence	Gradient	Hessian	Complexity
Gradient descent	✓	Linear	✓	✗	$\mathcal{O}(Td^2)$
Quasi-Newton	✗	Super linear	✓	✗	$\mathcal{O}(T^2d^2)$
Newton method	✗	Quadratic	✓	✓	$\mathcal{O}(Td^3)$
GEORCE	✓	Quadratic	✓	✗	$\mathcal{O}(Td^3)$

Table 1 Convergence, complexity, and use of higher order derivatives for different optimization algorithms in each iteration, where T is the number of grid points and d is the manifold dimension.

Comparison with other optimization methods

GEORCE has complexity $\mathcal{O}(Td^3)$ due to matrix inversions along the discretized curve but scales only linearly in T , unlike e.g. quasi-Newton methods (Table 1). Although the computational complexity in the manifold dimension is of a lower order for quasi-Newton methods and gradient descent, *GEORCE* exhibits faster convergence. Since the Hessian of the discretized energy functional in Eq. 5 is sparse, the update step in the Newton method can be simplified in complexity compared to the standard Newton method that has complexity $\mathcal{O}(T^3d^3)$ (see Appendix B.2). However, the sparse Newton step requires second-order derivatives, unlike *GEORCE*, which only requires first-order derivatives of the discretized energy.

4 Extension to Finslerian geometry

A Finsler geometry can be seen as a generalization of Riemannian geometry, where the tangent spaces are not equipped with an quadratic form metric but with a Finsler metric instead. A Finsler metric, $F : \mathcal{M} \times T\mathcal{M} \rightarrow \mathbb{R}_+$, where \mathcal{M} is a differentiable manifold, is a Minkowski norm in the sense that F is C^∞ on $T\mathcal{M} \setminus \{0\}$, $F(x, cv) = cF(x, v)$ for all $v \in T\mathcal{M}$, $x \in \mathcal{M}$ and $c > 0$ and for any $v \in T\mathcal{M}$, then $\frac{\partial^2 F}{\partial v^i \partial v^j}(x, v)$ is positive definite [50]. Geodesics on a Finsler manifold can be found equivalently to the Riemannian case by minimizing the energy functional, $\int_0^1 F^2(\gamma(t), \dot{\gamma}(t)) dt$, on a suitable set of curves connecting the two points thereby approximating a geodesic γ , [50]. *GEORCE* is similarly applicable to Finsler geometry. First, we note that the energy functional can be written as [50]

$$\frac{1}{2} \int_0^1 F^2(\gamma(t), \dot{\gamma}(t)) dt = \int_0^1 \dot{\gamma}(t)^\top G(\gamma(t), \dot{\gamma}(t)) \dot{\gamma}(t) dt, \quad (11)$$

where $G(x, v) = \frac{1}{2} \frac{\partial^2 F^2}{\partial v^i \partial v^j}(x, v)$ denotes the fundamental tensor in local coordinates², which is positive definite [50]. Unlike the Riemannian case, the fundamental tensor, G , is now a function of both the position and velocity, which implies the update formulas in Proposition 2. Similar to Riemannian case, we can formulate the discrete energy functional for the Finsler case as the following discretized energy functional in Eq. 11 becomes

$$E_F(x_{0:T}) := \min_{x_{0:T}} \sum_{t=0}^{T-1} (x_{t+1} - x_t)^\top G(x_t, x_{t+1} - x_t) (x_{t+1} - x_t) \quad (12)$$

s.t. $x_0 = a, x_T = b,$

where the corresponding discrete control problem becomes

$$\min_{(x_{1:T-1}, u_{0:T-1})} \sum_{t=0}^{T-1} u_t^\top G(x_t, u_t) u_t, \quad t = 0, \dots, T-1, \quad (13)$$

s.t. $x_{t+1} = x_t + u_t$
 $x_0 = a, x_T = b,$

Since, the fundamental tensor, G , depends on both the state, $x_{0:T}$, and control variable $u_{0:T}$, the necessary conditions in Proposition 1 have to be modified slightly to take this into account. Taking this into account and following the same approach as in the Riemannian case, we get the following update scheme in the Finslerian case (see Appendix A.4 for details)

$$\mu_{T-1} = \left(\sum_{t=0}^{T-1} G_t^{-1} \right)^{-1} \left(2(a-b) - \sum_{t=0}^{T-1} G_t^{-1} \left(\zeta_t + \sum_{t>j}^{T-1} \nu_j \right) \right),$$

$$u_t = -\frac{1}{2} G_t^{-1} \left(\mu_{T-1} + \zeta_t + \sum_{j>t}^{T-1} \nu_j \right), \quad t = 0, \dots, T-1, \quad (14)$$

$x_{t+1} = x_t + u_t, \quad t = 0, \dots, T-1,$
 $x_0 = a,$

where in iteration i we fix

$$\nu_t := \nabla_y (u_t^\top G(y, u_t) u_t) \Big|_{y=x_t^{(i)}, u_t=u_t^{(i)}}, \quad t = 1, \dots, T-1,$$

$$\zeta_t := \nabla_y (u_t^\top G(x_t, y) u_t) \Big|_{x_t=x_t^{(i)}, u_t=u_t^{(i)}, y=u_t^{(i)}}, \quad t = 1, \dots, T-1,$$

$$G_t := G(x_t^{(i)}, u_t^{(i)}), \quad t = 0, \dots, T-1.$$

²In literature, the fundamental tensor is often denoted with a lower case g . To have the notation consistent with the Riemannian case, we opt to use an upper case G instead.

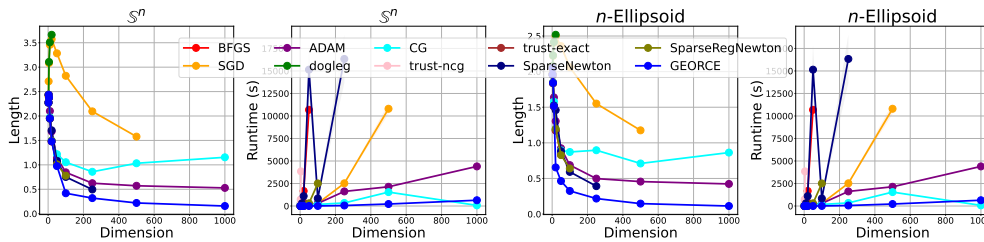


Fig. 4 The first two figures display the length and runtime of geodesics for \mathbb{S}^n estimated using different algorithms from Table 2 and other methods in Appendix E.3. The latter row shows the length and runtime, respectively for the n -Ellipsoid with half axes of n equally spaced points between 0.5 and 1.0. The optimization solvers are described in Appendix E.1.

We see that the only extra term in *GEORCE* for Finsler manifolds is $\{\zeta_t\}_{t=0}^{T-1}$. Using the modified update scheme in Eq. 14, we estimate geodesics for Finsler manifolds similar to Algorithm 1. For completeness, we show the algorithm in pseudo-code for the Finsler case in Appendix B.1.

Using the same technique as in the Riemannian case, we show that *GEORCE* for Finsler manifolds has global convergence and local quadratic convergence. We refer to the details in Appendix A.7.

5 Experiments

Riemannian manifolds

To compare *GEORCE* with other optimization algorithms, we show the runtime and length of geodesics computed for different manifolds with varying dimensions in Table 2. Here we compare *GEORCE* with *BFGS* [37–40] and *ADAM* [41]. We terminate the algorithm if the ℓ^2 -norm of the gradient of the discretized energy functional in Eq. 5 is less than 10^{-4} , or if the number of iterations exceeds 1,000. A full description of the manifolds and experimental details can be found in Appendix C and Appendix E, respectively.

We show the estimated geodesics with $T = 100$ grid points and summarize the results for the corresponding runtime and length of the computed geodesics for the n -sphere and n -ellipsoid in Fig. 4. In Appendix E.3, we show similar runtime experiments for varying grid points as well as other optimization algorithms. We also show the corresponding results on a GPU with other CUDA compatible algorithms. In general, we see that *GEORCE* is considerably faster with lower length compared to alternative methods.

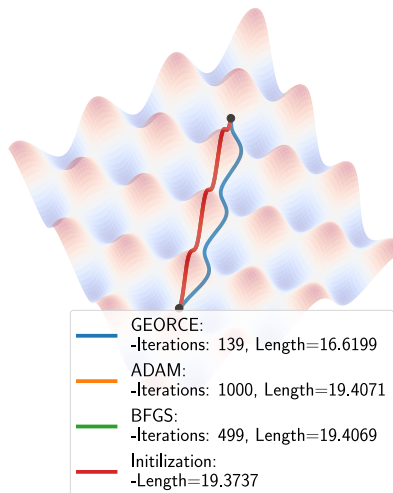


Fig. 5 The geodesics for an “egg-tray” parameterized by $(x, y, 2 \cos x \cos y)$, where there are no unique geodesic connecting the points. The *BFGS* estimate, *ADAM* estimate and the initial curve overlap completely.

Riemannian Manifold	BFGS (T=100)			ADAM (T=100)			GEORCE (T=100)		
	Length	Runtime	Length	Runtime	Length	Runtime	Length	Runtime	
\mathbb{S}^2	2.2742	57.4164 ± 0.0616	2.2772	0.2335 ± 0.0005	2.2741	0.0078 ± 0.0000			
\mathbb{S}^3	2.4342	67.4657 ± 0.4874	2.4377	0.3475 ± 0.0010	2.4342	0.0635 ± 0.0001			
\mathbb{S}^5	2.3757	77.6975 ± 0.0741	2.4222	1.9894 ± 0.0188	2.3755	0.2219 ± 0.0001			
\mathbb{S}^{10}	1.9529	150.0621 ± 0.8919	2.1016	4.4208 ± 0.0308	1.9523	0.3184 ± 0.0002			
\mathbb{S}^{20}	1.4810	1068.8645 ± 17.2001	1.6839	8.7097 ± 0.0352	1.4808	0.6732 ± 0.0204			
\mathbb{S}^{50}	1.0464	7350.6001 ± 244.3737	1.1463	61.8926 ± 0.3034	0.9749	4.1016 ± 0.0201			
\mathbb{S}^{100}	—	—	0.8466	277.4217 ± 0.2280	0.4187	10.9208 ± 0.0071			
\mathbb{S}^{250}	—	—	0.6244	1424.9031 ± 22.1592	0.3192	78.2937 ± 0.0091			
\mathbb{S}^{500}	—	—	0.5717	2242.4697 ± 17.9769	0.2198	224.2761 ± 0.4894			
\mathbb{S}^{1000}	—	—	0.5279	4329.6621 ± 38.0163	0.1573	893.4682 ± 7.3130			
E (2)	1.9595	56.9650 ± 0.4106	1.9596	0.2328 ± 0.0001	1.9595	0.0067 ± 0.0001			
E (3)	2.0499	94.1769 ± 0.7044	2.0525	0.3392 ± 0.0024	2.0501	0.0119 ± 0.0000			
E (5)	1.8403	194.5403 ± 1.3293	1.9521	2.2227 ± 0.0186	1.8410	0.4220 ± 0.0038			
E (10)	1.5114	427.6278 ± 4.1044	1.6384	4.5697 ± 0.0541	1.5139	0.4566 ± 0.0016			
E (20)	1.1795	1669.2692 ± 10.2877	1.3049	9.4335 ± 0.0507	0.6548	1.9786 ± 0.0031			
E (50)	0.8338	10685.6133 ± 321.6447	0.9244	73.5682 ± 0.3306	0.4642	2.4208 ± 0.0222			
E (100)	—	—	0.6872	289.4196 ± 2.5224	0.3249	7.7128 ± 0.0714			
E (250)	—	—	0.4978	1620.6428 ± 16.9546	0.2178	56.8527 ± 0.1526			
E (500)	—	—	0.4559	2135.6899 ± 30.5699	0.1467	220.1656 ± 0.9902			
E (1000)	—	—	0.4232	4398.9453 ± 25.8738	0.1131	641.7199 ± 20.9901			
\mathbb{T}^2	9.9851	92.7400 ± 3.1267	9.9855	0.1060 ± 0.0002	9.9851	0.0182 ± 0.0003			
\mathbb{H}^2	1.2499	75.0079 ± 0.1710	1.2499	0.0988 ± 0.0001	1.2498	0.0025 ± 0.0001			
\mathcal{P} (2)	1.0669	88.2739 ± 0.4152	1.0879	0.2611 ± 0.0004	1.0669	0.0141 ± 0.0001			
\mathcal{P} (3)	2.2639	168.5082 ± 0.3039	2.2896	2.3780 ± 0.0046	2.2639	0.1442 ± 0.0002			
Gaussian Distribution	2.5952	47.6288 ± 0.1359	2.5956	0.0167 ± 0.0001	2.5952	0.0015 ± 0.0000			
Fréchet Distribution	1.1538	51.3063 ± 0.0566	1.1542	0.0185 ± 0.0001	1.1539	0.0009 ± 0.0000			
Cauchy Distribution	1.6454	36.5031 ± 0.0437	1.6466	0.0177 ± 0.0001	1.6452	0.0020 ± 0.0000			
Pareto Distribution	0.8297	39.0465 ± 0.0471	0.8336	0.0168 ± 0.0000	0.8297	0.0007 ± 0.0000			

Table 2 The length of the estimated geodesics for the *BFGS*-algorithm, *ADAM* and *GEORCE* on a CPU. The methods were terminated if the ℓ^2 -norm of the gradient was less than 10^{-4} or after 1,000 iterations. $E(n)$ denotes an Ellipsoid of dimension n with half axes of n equally spaced points between 0.5 and 1.0, while $\mathcal{P}(n)$ denotes the space of $n \times n$ symmetric positive definite matrices. When the computational time was longer than 24 hours, the value is set to —.

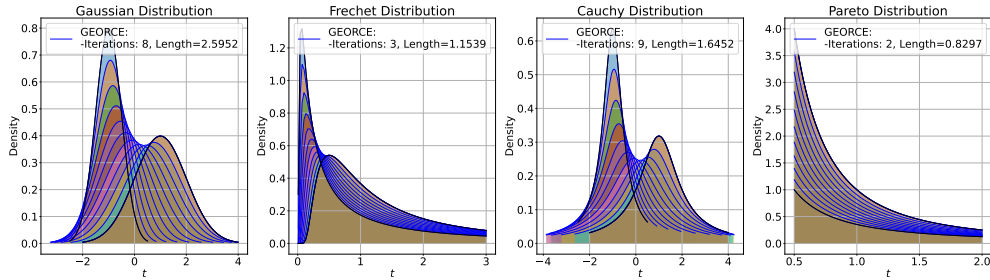


Fig. 6 The connecting geodesic between four different distributions equipped with the Fisher-Rao metric using *GEORCE*. From left to right the figures show the connecting geodesic (blue) between two fixed distributions (black) for the Gaussian distribution, Fréchet distribution, Cauchy distribution and the Pareto distribution.

To test *GEORCE* on manifolds with multiple length minimizing geodesics, we consider the geodesic between $(-5, -5)$ and $(5, 5)$ on an “egg-tray” parameterized by $(x, y, 2 \cos x \cos y)$ with $T = 1,000$ grid points. We show the estimates in Fig. 5, where we see that *GEORCE* obtains the a significantly smaller length, where there is also a clear symmetric to solution to *GEORCE* along the other side of the “egg-tops”.

To illustrate the application of *GEORCE* to more abstract manifolds, we compute geodesics on the statistical manifolds, i.e., between distributions [17, 18]. Fig. 6 shows the estimated geodesic between a Gaussian distribution, a Fréchet distribution, a Cauchy distribution, and a Pareto distribution using *GEORCE* all equipped with the Fisher-Rao metric in eq. 4. The metric matrix function for the corresponding statistical manifold is described in [31]. We see that *GEORCE* converges after only a few iterations. The computed geodesics using alternative methods are summarized in Table 2, where we see that *GEORCE* obtains significantly shorter length much faster, also in high-dimension, compared to alternative methods.

We further illustrate the application of *GEORCE* to information geometry by considering potential functions encountered in Bregman geometry [18]. We consider the log-partition function for the Gaussian distribution, which is convex and smooth

$$A(\theta_1, \theta_2) = \frac{\theta_1^2}{2\theta_2} + \frac{1}{2} \log \left(\frac{2\pi}{\theta_2} \right),$$

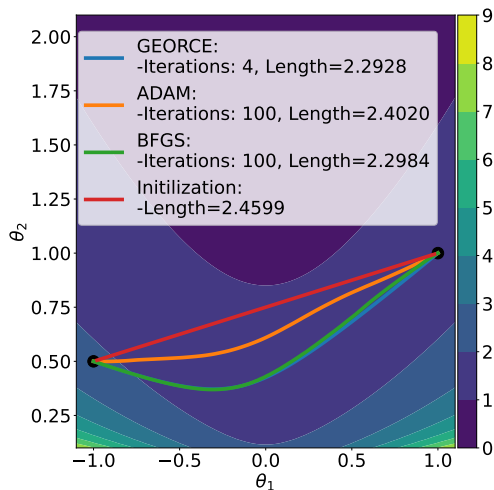


Fig. 7 The geodesics computed under the Hessian of the log-partition function of a Gaussian distribution. The background color illustrates the log-partition function.

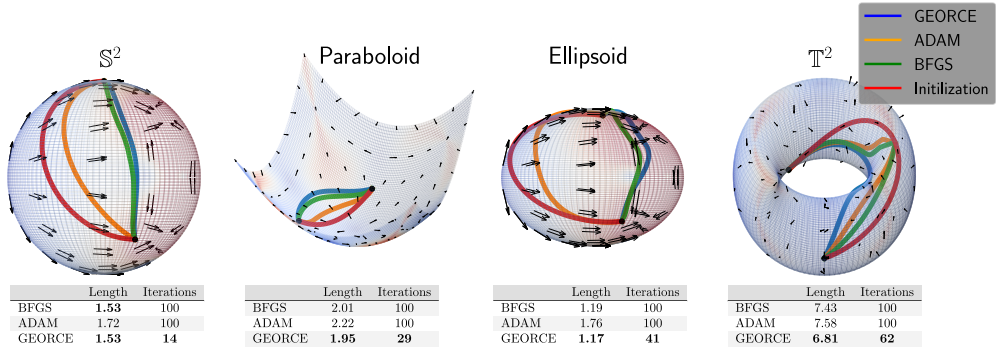


Fig. 8 Comparison between *GEORCE* and baseline methods for computing geodesics on four different Finsler manifolds. The Finsler metrics stem from a Riemannian background metric with the force field in eq. 15 on them. The length of the force field is displayed in color, while the arrows show the direction of the force field. The algorithms are terminated if the ℓ^2 -norm of the gradient of the discretized energy functional is less than 10^{-4} , or if the number of iterations exceeds 100. We see that *GEORCE* uses less iterations and obtains the smallest length.

where $\theta_1 = \frac{\mu}{\sigma^2}$ and $\theta_2 = \frac{1}{\sigma^2}$ for a Gaussian distribution with parameters (μ, σ) such that the density takes the form of an exponential family $p(x) = h(x) \exp(\theta_1 x - A(\theta_1, \theta_2))$ for a suitable h . We consider the corresponding Hessian of the log-partition function, which defines a Riemannian metric. Fig. 7 shows geodesics computed with both *GEORCE* and alternative methods using at most 100 iterations. We see that *GEORCE* uses less iterations and obtains the smallest length compared to the alternative methods.

Finsler manifolds

To illustrate our method for different Finsler manifolds and dimensions, we consider a microswimmer on a Riemannian manifold m that moves with constant self-propulsion velocity v with Riemannian length, $v_0 := \|v\|_g$ [51] and we assume that this movement is affected by a generic force field, f , of the form

$$f(x) = \frac{\sin x \odot \cos x}{(\cos x)^\top G(x) \cos x}, \quad (15)$$

where $\cos x$ and $\sin x$ denote the element-wise function for each entry of the local coordinates x , while G denotes the corresponding Riemannian background metric such that the force field has G -length less than or equal to 1. If $\|f(x)\|_g < v_0$, then the optimal travel time of the microswimmer corresponds to a geodesic for a Finsler manifold of the form [51]

$$F = \sqrt{a_{ij} \dot{r}^i \dot{r}^j} + b_i \dot{r}^i,$$

where $a_{ij} = g_{ij} \lambda + f_i f_j \lambda^2$, $b_i = -f_i \lambda$, $b_i = -f_i \lambda$, $f_i = g_{ij} f^j$ and $\lambda^{-1} = v_0^2 - g_{ij} f^i f^j$ [51], while $r(t)$ denotes the position of the microswimmer at time t . We refer to [51] and Appendix C for details. We consider the same background metrics in Table 2 all equipped with the generic force field in eq. 15 and compare *GEORCE* to *BFGS* [37–40] and *ADAM* [41]. Fig. 8 shows the estimated geodesics for four different Riemannian

Finsler Manifold	BFGS (T=100)			ADAM (T=100)			GEORCE (T=100)		
	Length	Runtime	Length	Runtime	Length	Runtime	Length	Runtime	
\mathbb{S}^2	1.6525	244.9129 ± 0.0680	1.6536	0.4967 ± 0.0007	1.6525	0.0194 ± 0.0009			
\mathbb{S}^3	1.7433	277.8015 ± 0.5819	1.7456	0.7639 ± 0.0031	1.7432	0.0362 ± 0.0001			
\mathbb{S}^5	1.7032	435.6987 ± 4.6022	1.7377	4.6711 ± 0.0047	1.7029	0.4556 ± 0.0021			
\mathbb{S}^{10}	1.4151	812.2809 ± 13.5968	1.5174	9.7974 ± 0.0052	1.4109	0.7473 ± 0.0029			
\mathbb{S}^{20}	1.0951	1446.0956 ± 4.8038	1.2018	18.3489 ± 0.0747	1.0760	1.2856 ± 0.0016			
\mathbb{S}^{50}	0.8216	5992.7261 ± 56.5973	0.8128	146.4556 ± 0.9341	0.7285	8.4758 ± 0.0234			
\mathbb{S}^{100}	—	—	0.6187	498.9705 ± 0.4032	0.2570	15.3786 ± 0.0092			
\mathbb{S}^{250}	—	—	0.5195	1397.6732 ± 0.7793	0.1622	132.5889 ± 0.1106			
\mathbb{S}^{500}	—	—	0.4850	1954.3231 ± 14.1107	0.1404	364.5326 ± 1.8222			
\mathbb{S}^{1000}	—	—	0.3843	5982.0884 ± 204.1833	0.1140	1338.9869 ± 2.3954			
E (2)	1.3616	230.0809 ± 1.3967	1.3621	0.5310 ± 0.0025	1.3618	0.0130 ± 0.0002			
E (3)	1.4001	416.6281 ± 5.5354	1.4087	0.8183 ± 0.0026	1.4023	0.1081 ± 0.0001			
E (5)	1.2951	638.7185 ± 2.7818	1.3265	4.3802 ± 0.0039	1.2956	0.4554 ± 0.0014			
E (10)	1.0733	741.9274 ± 12.3382	1.1229	9.7899 ± 0.0117	1.0804	0.5815 ± 0.0022			
E (20)	0.8510	1820.3137 ± 4.0734	0.8980	19.4614 ± 0.0039	0.8121	1.0671 ± 0.0044			
E (50)	0.5981	11191.9424 ± 597.7002	0.6325	146.6409 ± 0.1668	0.2842	4.4377 ± 0.0451			
E (100)	—	—	0.4936	491.8223 ± 0.2346	0.2009	14.5367 ± 0.0092			
E (250)	—	—	0.4159	1475.5049 ± 4.1430	0.1287	125.4187 ± 0.0888			
E (500)	—	—	0.4142	1984.7845 ± 10.5689	0.0967	373.2816 ± 0.4227			
E (1000)	—	—	0.3444	5929.4438 ± 167.1873	0.0799	1211.8812 ± 0.2511			
\mathbb{T}^2	7.3890	449.4798 ± 10.3282	7.3585	0.3294 ± 0.0018	6.8067	0.1126 ± 0.0002			
\mathbb{H}^2	1.3340	384.3149 ± 0.3044	1.3360	0.2744 ± 0.0024	1.3337	0.0094 ± 0.0001			
\mathcal{P} (2)	0.7291	414.8355 ± 3.0837	0.7338	0.6368 ± 0.0026	0.7292	0.0222 ± 0.0001			
\mathcal{P} (3)	1.2856	536.6575 ± 0.9323	1.2980	5.2824 ± 0.0540	1.2856	0.2094 ± 0.0004			
Gaussian Distribution	1.6878	163.4399 ± 0.1859	1.6936	0.1145 ± 0.0001	1.6878	0.0047 ± 0.0001			
Fréchet Distribution	0.5408	123.8418 ± 0.0499	0.5406	0.0585 ± 0.0001	0.5405	0.0021 ± 0.0001			
Cauchy Distribution	1.1134	182.3980 ± 2.2559	1.1133	0.1105 ± 0.0007	1.1133	0.0067 ± 0.0002			
Pareto Distribution	0.3884	84.8186 ± 0.0832	0.3885	0.0235 ± 0.0007	0.3883	0.0020 ± 0.0001			

Table 3 The length of the estimated geodesics for the *BFGS*-algorithm, *ADAM*-gradient descent and *GEORCE* on a CPU. The algorithms have been stopped if the ℓ^2 -norm of the gradient was less than 10^{-4} or if a maximum of 1,000 iterations have been reached. $E(n)$ denotes an Ellipsoid of dimension n with half axes of n equally spaced points between 0.5 and 1.0, while $\mathcal{P}(n)$ denotes the space of $n \times n$ symmetric positive definite matrices. When the computational time was longer than 24 hours, the value is set to —.

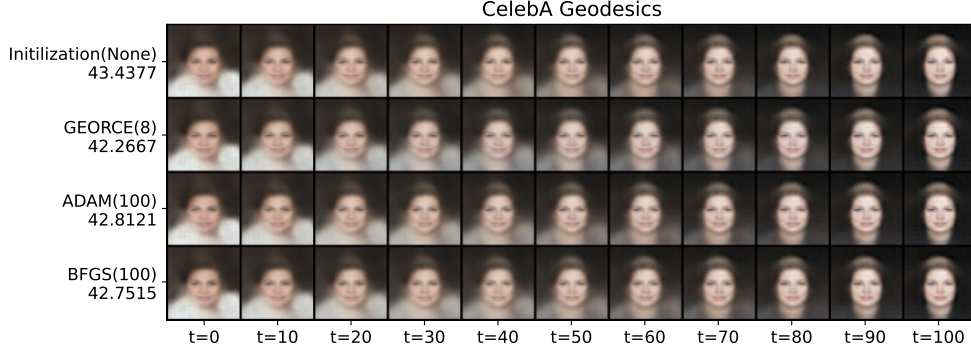


Fig. 9 Geodesics for a variational autoencoder [52] trained on the CelebA dataset [53] using *GEORCE* and alternative methods. All algorithms are terminated if the ℓ^2 -norm of the gradient of the discretized energy functional in eq. 5 is less than 10^{-3} , or if the number of iterations exceeds 100. The algorithms are written to the left with number of iterations in parenthesis and length to the right. The first-axis shows the grid number for the image sequence. The details of the manifolds and experiments can be found Appendix D.1

manifolds equipped with the generic force field in eq. 15. We show the estimated geodesics for $T = 100$ grid points in Table 3. In Appendix E.3 we show similar runtime experiments for varying grid points as well as other optimization algorithms. We see that *GEORCE* is considerably faster and more accurate than the alternatives.

Applications to generative models

To illustrate the application of *GEORCE* to learned manifolds, we compute geodesics for generative models and compare them to similar methods. A variational autoencoder (VAE) is a generative model that learns the data distribution, $\mathcal{X} \subset \mathbb{R}^D$, and a latent representation of data, $\mathcal{Z} \subset \mathbb{R}^d$, with $d < D$ by maximizing a lower bound of the log-likelihood of the data with respect to a variational family of distributions [52]

For latent space generative models, the *decoder* can be seen as a smooth d dimensional immersion, $f : \mathcal{Z} \rightarrow \mathcal{X}$, which defines a Riemannian geometry with the pull-back metric $G(z) = J_f^\top(z)J_f(z)$, where J_f denotes the Jacobian of z [11, 12].

We train a VAE for the CelebA dataset [53], which consists of 202,599 facial images of size $64 \times 64 \times 3$, where the architecture is described in Appendix D.1. Fig. 9 illustrates the geodesics constructed between two images reconstructed using the variational autoencoder. We see that *GEORCE* obtains a smaller length than comparable methods for $T = 100$ grid points. We refer to Appendix D.2 for runtime results for the VAE, where we see that *GEORCE* is significantly faster than alternative methods. Note that the tolerance for convergence is 10^{-3} , since it was observed that it was not possible for any method to obtain an ℓ^2 -norm of the gradient less than 10^{-4} . This is most likely due to potential instabilities for the learned manifold. We summarize the results in Table E8 in Appendix E.3, where we also consider the geodesic with a VAE trained on MNIST data [54] and SVHN data [55]. For the exact architecture and further experiments of the VAE, we refer to Appendix D.1 and Appendix D.2.

6 Conclusion

In this paper, we have introduced the algorithm *GEORCE* for estimating geodesics between any given points on Riemannian and Finsler manifolds by formulating the discretized energy functional as a control problem. We have proved that *GEORCE* has global convergence and quadratic local convergence, and thus, *GEORCE* exhibits similar global convergence as gradient descent as well as local quadratic convergence similar to the Newton method without using second order derivatives. *GEORCE* scales cubically in the manifold dimension and only linearly in the number of grid points. Empirically, we have shown that *GEORCE* exhibits superior convergence in terms of runtime and accuracy compared to other geodesic optimization algorithms for Riemannian and Finsler manifolds across both dimensions and manifolds.

Limitations: *GEORCE* exhibits both global convergence and local quadratic convergence requiring few iterations. However, *GEORCE* requires evaluating the inverse matrix of the metric matrix function in each iteration, which can be numerically expensive. In addition, *GEORCE* uses line search to determine the step size in each iteration, and if it is numerically expensive to evaluate the discretized energy functional, then this can potentially increase the runtime of *GEORCE*. Further research should therefore investigate efficient approximations of the inverse metric matrix function as well as possible adaptive updating schemes for the step size to increase computational efficiency for high-dimensional problems.

Supplementary information. The supplementary information in the paper consists of the appendix for proofs, details on experiments and manifolds as well as additional experiments.

Acknowledgements. Many thanks to Prof. Steen Markvorsen and Dr. Andreas A. Bock for comments and corrections in the process of writing this paper. Especially, a thanks to Prof. Steen Markvorsen for hinting at the possible extension to Finsler geometry. SH is supported by a research grant (42062) from VILLUM FONDEN. This project received funding from the European Research Council (ERC) under the European Union’s Horizon research and innovation programme (grant agreement 101125993). The work was partly funded by the Novo Nordisk Foundation through the Center for Basic Machine Learning Research in Life Science (NNF20OC0062606).

Declarations

- Funding: Research grant 42062 from VILLUM FONDEN; funding from the European Research Council (ERC) under the European Union’s Horizon research and innovation programme (grant agreement 101125993); funding from the Novo Nordisk Foundation through the Center for Basic Machine Learning Research in Life Science (NNF20OC0062606).
- Conflict of interest/Competing interests (check journal-specific guidelines for which heading to use): NA
- Ethics approval and consent to participate: NA
- Consent for publication: Currently under review.
- Data availability: All data used are described in the appendix.

- Materials availability: NA
- Code availability: The code can be found at <https://github.com/FrederikMR/georce>
- Author contribution: FMR derived the algorithm and implemented the method as well as benchmarks. SH supervised the project with comments and corrections. The paper was written jointly by SH and FMR. All authors reviewed the manuscript.

References

- [1] Pennec, X., Sommer, S. & Fletcher, T. *Riemannian Geometric Statistics in Medical Image Analysis* (Academic Press, 2019).
- [2] Pennec, X., Ayache, N. & Thirion, J.-P. *Landmark-based registration using features identified through differential geometry*, 499–513 (Academic Press, Inc., USA, 2000).
- [3] Lenglet, C., Rousson, M., Deriche, R. & Faugeras, O. Statistics on multivariate normal distributions: A geometric approach and its application to diffusion tensor mri. *Rapport de recherche, Institut National de Recherche en Informatique et en Automatique (INRIA)* (2004).
- [4] Watson, J. L. *et al.* Broadly applicable and accurate protein design by integrating structure prediction networks and diffusion generative models. *bioRxiv* (2022). URL <https://www.biorxiv.org/content/early/2022/12/10/2022.12.09.519842>.
- [5] Detlefsen, N., Hauberg, S. & Boomsma, W. Learning meaningful representations of protein sequences. *Nature Communications* **13** (2022). Publisher Copyright: © 2022, The Author(s).
- [6] Shapovalov, M. & Dunbrack, R. A smoothed backbone-dependent rotamer library for proteins derived from adaptive kernel density estimates and regressions. *Structure (London, England : 1993)* **19**, 844–58 (2011).
- [7] Beik-Mohammadi, H., Hauberg, S., Arvanitidis, G., Neumann, G. & Rozo, L. Learning riemannian manifolds for geodesic motion skills (2021). URL <https://arxiv.org/abs/2106.04315>. arXiv:2106.04315.
- [8] Simeonov, A. *et al.* Neural descriptor fields: Se(3)-equivariant object representations for manipulation (2021). URL <https://arxiv.org/abs/2112.05124>. arXiv:2112.05124.
- [9] Senanayake, R. & Ramos, F. T. Directional grid maps: Modeling multimodal angular uncertainty in dynamic environments. *2018 IEEE/RSJ International Conference on Intelligent Robots and Systems (IROS)* 3241–3248 (2018). URL <https://api.semanticscholar.org/CorpusID:52158241>.
- [10] Feiten, W., Lang, M. & Hirche, S. Rigid motion estimation using mixtures of projected gaussians 1465–1472 (2013).

- [11] Arvanitidis, G., Hansen, L. K. & Hauberg, S. Latent space oddity: on the curvature of deep generative models (2018). URL <https://arxiv.org/abs/1710.11379>. arXiv:1710.11379.
- [12] Shao, H., Kumar, A. & Fletcher, P. T. The riemannian geometry of deep generative models (2017). arXiv:1711.08014.
- [13] Bortoli, V. D. *et al.* Riemannian score-based generative modelling (2022). URL <https://arxiv.org/abs/2202.02763>. arXiv:2202.02763.
- [14] Jo, J. & Hwang, S. J. Generative modeling on manifolds through mixture of riemannian diffusion processes (2024). URL <https://arxiv.org/abs/2310.07216>. arXiv:2310.07216.
- [15] Mathieu, E. & Nickel, M. Riemannian continuous normalizing flows (2020). URL <https://arxiv.org/abs/2006.10605>. arXiv:2006.10605.
- [16] Rozen, N., Grover, A., Nickel, M. & Lipman, Y. Moser flow: divergence-based generative modeling on manifolds (2021).
- [17] Arvanitidis, G., González-Duque, M., Pouplin, A., Kalatzis, D. & Hauberg, S. Pulling back information geometry (2022). URL <https://arxiv.org/abs/2106.05367>. arXiv:2106.05367.
- [18] Nielsen, F. An elementary introduction to information geometry. *Entropy* **22**, 1100 (2020). URL <http://dx.doi.org/10.3390/e22101100>.
- [19] Cheng, C., Li, J., Peng, J. & Liu, G. Categorical flow matching on statistical manifolds (2025). URL <https://arxiv.org/abs/2405.16441>. arXiv:2405.16441.
- [20] Myers, V., Ellis, E., Levine, S., Eysenbach, B. & Dragan, A. Learning to assist humans without inferring rewards (2025). URL <https://arxiv.org/abs/2411.02623>. arXiv:2411.02623.
- [21] Davis, O. *et al.* Fisher flow matching for generative modeling over discrete data (2024). URL <https://arxiv.org/abs/2405.14664>. arXiv:2405.14664.
- [22] Hauberg, S. *Differential geometry for generative modeling* (2025).
- [23] do Carmo, M. *Riemannian Geometry* Mathematics (Boston, Mass.) (Birkhäuser, 1992). URL <https://books.google.dk/books?id=uXJQQgAACAAJ>.
- [24] Detlefsen, N. S. *et al.* Stochman. *GitHub*. Note: <https://github.com/MachineLearningLifeScience/stochman/> (2021).
- [25] Arvanitidis, G., Hansen, L. K. & Hauberg, S. Latent space oddity: on the curvature of deep generative models (2021). arXiv:1710.11379.

- [26] Noakes, L. A global algorithm for geodesics. *Journal of the Australian Mathematical Society. Series A. Pure Mathematics and Statistics* **65**, 37–50 (1998).
- [27] Tosi, A., Hauberg, S., Vellido, A. & Lawrence, N. D. Metrics for probabilistic geometries (2014). URL <https://arxiv.org/abs/1411.7432>. arXiv:1411.7432.
- [28] Nash, J. C1 isometric imbeddings. *Annals of Mathematics* **60**, 383–396 (1954). URL <http://www.jstor.org/stable/1969840>.
- [29] Whitney, H. Differentiable manifolds. *Annals of Mathematics* **37**, 645–680 (1936). URL <http://www.jstor.org/stable/1968482>.
- [30] Gallot, S., Hulin, D. & Lafontaine, J. *Riemannian Geometry* Universitext (Springer Berlin Heidelberg, 2004). URL <https://books.google.dk/books?id=6F4Umpws.gUC>.
- [31] Miyamoto, H. K., Meneghetti, F. C. C., Pinele, J. & Costa, S. I. R. On closed-form expressions for the fisher-rao distance (2024). URL <https://arxiv.org/abs/2304.14885>. arXiv:2304.14885.
- [32] Peter, A. & Rangarajan, A. Shape analysis using the fisher-rao riemannian metric: Unifying shape representation and deformation. *In: IEEE ISBI. IEEE* **2006**, 1164–1167 (2006).
- [33] Luenberger, D. & Ye, Y. *Linear and Nonlinear Programming* International Series in Operations Research & Management Science (Springer US, 2008). URL <https://books.google.dk/books?id=-pD62uvi9lgC>.
- [34] Kaya, C. Y. & Noakes, J. L. Leapfrog for optimal control. *SIAM Journal on Numerical Analysis* **46**, 2795–2817 (2008). URL <https://doi.org/10.1137/060675034>.
- [35] Hennig, P. & Hauberg, S. Probabilistic solutions to differential equations and their application to riemannian statistics (2014). URL <https://arxiv.org/abs/1306.0308>. arXiv:1306.0308.
- [36] Arvanitidis, G., Hauberg, S., Hennig, P. & Schober, M. Fast and robust shortest paths on manifolds learned from data (2019). URL <https://arxiv.org/abs/1901.07229>. arXiv:1901.07229.
- [37] Broyden, C. G. The Convergence of a Class of Double-rank Minimization Algorithms 1. General Considerations. *IMA Journal of Applied Mathematics* **6**, 76–90 (1970). URL <https://doi.org/10.1093/imamat/6.1.76>.
- [38] Fletcher, R. A new approach to variable metric algorithms. *The Computer Journal* **13**, 317–322 (1970). URL <https://doi.org/10.1093/comjnl/13.3.317>.

- [39] Goldfarb, D. A family of variable-metric methods derived by variational means. *Mathematics of Computation* **24**, 23–26 (1970). URL <https://api.semanticscholar.org/CorpusID:790344>.
- [40] Shanno, D. & Kettler, P. Optimal conditioning of quasi-newton methods. *Mathematics of Computation - Math. Comput.* **24**, 657–657 (1970).
- [41] Kingma, D. P. & Ba, J. Adam: A method for stochastic optimization (2017). [arXiv:1412.6980](https://arxiv.org/abs/1412.6980).
- [42] Crane, K., Livesu, M., Puppo, E. & Qin, Y. A survey of algorithms for geodesic paths and distances (2020). [arXiv:2007.10430](https://arxiv.org/abs/2007.10430).
- [43] Surazhsky, V., Surazhsky, T., Kirsanov, D., Gortler, S. J. & Hoppe, H. Fast exact and approximate geodesics on meshes. *ACM Trans. Graph.* **24**, 553–560 (2005). URL <https://doi.org/10.1145/1073204.1073228>.
- [44] Chen, J. & Han, Y. Shortest paths on a polyhedron. *Proceedings of the Sixth Annual Symposium on Computational Geometry* 360–369 (1990). URL <https://doi.org/10.1145/98524.98601>.
- [45] Xin, S.-Q. & Wang, G.-J. Improving chen and han’s algorithm on the discrete geodesic problem. *ACM Trans. Graph.* **28** (2009).
- [46] Qin, Y., Han, X., Yu, H., Yu, Y. & Zhang, J. Fast and exact discrete geodesic computation based on triangle-oriented wavefront propagation. *ACM Trans. Graph.* **35** (2016). URL <https://doi.org/10.1145/2897824.2925930>.
- [47] Beik-Mohammadi, H., Hauberg, S., Arvanitidis, G., Neumann, G. & Rozo, L. Learning riemannian manifolds for geodesic motion skills (2021).
- [48] Wolfe, P. Convergence conditions for ascent methods. *SIAM Review* **11**, 226–235 (1969). URL <https://doi.org/10.1137/1011036>.
- [49] Armijo, L. Minimization of functions having lipschitz continuous first partial derivatives. *Pacific Journal of Mathematics* **16**, 1–3 (1966).
- [50] Ohta, S. *Comparison Finsler Geometry* Springer Monographs in Mathematics (Springer International Publishing, 2021). URL <https://books.google.dk/books?id=4Mh6zgEACAAJ>.
- [51] Piro, L., Tang, E. & Golestanian, R. Optimal navigation strategies for microswimmers on curved manifolds. *Physical Review Research* **3** (2021). URL <http://dx.doi.org/10.1103/PhysRevResearch.3.023125>.
- [52] Kingma, D. P. & Welling, M. Auto-encoding variational bayes (2022). URL <https://arxiv.org/abs/1312.6114>. [arXiv:1312.6114](https://arxiv.org/abs/1312.6114).

- [53] Liu, Z., Luo, P., Wang, X. & Tang, X. Deep learning face attributes in the wild. *Proceedings of International Conference on Computer Vision (ICCV)* (2015).
- [54] Deng, L. The mnist database of handwritten digit images for machine learning research. *IEEE Signal Processing Magazine* **29**, 141–142 (2012).
- [55] Netzer, Y. *et al.* Reading digits in natural images with unsupervised feature learning. *NIPS Workshop on Deep Learning and Unsupervised Feature Learning 2011* (2011). URL http://ufldl.stanford.edu/housenumbers/nips2011_housenumbers.pdf.
- [56] Kirk, D. *Optimal Control Theory: An Introduction* Dover Books on Electrical Engineering Series (Dover Publications, 2004). URL <https://books.google.dk/books?id=fCh2SAtWIdwC>.
- [57] Thomas, L. Elliptic problems in linear difference equations over a network (1949).
- [58] Noakes, L. & Zhang, E. Finding geodesics joining given points. *Advances in Computational Mathematics* **48** (2022).
- [59] Ruder, S. An overview of gradient descent optimization algorithms (2017). URL <https://arxiv.org/abs/1609.04747>. arXiv:1609.04747.
- [60] Nocedal, J. & Wright, S. *Numerical Optimization* Springer Series in Operations Research and Financial Engineering (Springer New York, 2006). URL <https://books.google.dk/books?id=VbHYoSyeIFcC>.
- [61] Virtanen, P. *et al.* SciPy 1.0: Fundamental Algorithms for Scientific Computing in Python. *Nature Methods* **17**, 261–272 (2020).
- [62] Dormand, J. & Prince, P. A family of embedded runge-kutta formulae. *Journal of Computational and Applied Mathematics* **6**, 19–26 (1980). URL <https://www.sciencedirect.com/science/article/pii/0771050X80900133>.
- [63] Bogacki, P. & Shampine, L. A 3(2) pair of runge - kutta formulas. *Applied Mathematics Letters* **2**, 321–325 (1989). URL <https://www.sciencedirect.com/science/article/pii/0893965989900797>.
- [64] Hairer, E., Norsett, S. & Wanner, G. *Solving Ordinary Differential Equations I: Nonstiff Problems* Vol. 8 (1993).
- [65] Hairer, E. & Wanner, G. *Solving Ordinary Differential Equations II. Stiff and Differential-Algebraic Problems* Vol. 14 (1996).
- [66] Shampine, L. F. & Reichelt, M. W. The matlab ode suite. *SIAM Journal on Scientific Computing* **18**, 1–22 (1997). URL <https://doi.org/10.1137/S1064827594276424>.

- [67] Hindmarsh, A. C. Stepleman, R. S. (ed.) *ODEPACK, a systematized collection of ODE solvers*. (ed. Stepleman, R. S.) *Scientific Computing*, 55–64 (North-Holland, Amsterdam, 1983).

Appendix A Proofs and derivations

A.1 Assumptions

In the following, we will prove local quadratic convergence under the following assumptions.

Assumption 5 *We assume the following regarding the discretized energy functional.*

- A (local) minimum point $z^* = (x^*, u^*)$ to the discretized energy functional is defined as strongly unique minimum point if and only if

$$\exists \epsilon > 0 : \quad \exists K > 0 : \quad \forall z \in B_\epsilon(z^*) : \quad E(z) - E(z^*) \geq K \|z - z^*\|,$$

where $B_\epsilon(z^*) = \{z \mid \|z - z^*\| < \epsilon\}$.

- We assume that the discretized energy functional $E(z)$ is locally Lipschitz.
- The first order Taylor approximation of the discretized energy functional is

$$\Delta E = \langle \nabla E(z_0), \Delta z \rangle + \mathcal{O}(\Delta z) \|\Delta z\|,$$

i.e., we assume that $\mathcal{O}(\Delta z)$ is independent of z_0 , and the term $\mathcal{O}(\Delta z) \|\Delta z\|$ can be re-written as $\tilde{\mathcal{O}}(\|\Delta z\|^2)$ locally (which follows from the Lipschitz condition).

Further for global convergence we will assume Lipschitz continuity of the discretized energy functional. Note that since the metric varies smoothly on the manifold, then the discretized energy functional is also smooth and hence Lipschitz. Thus, all Finsler and Riemannian manifolds satisfies the above conditions, but an even larger class of energy functionals that does not necessarily stem from a Riemannian or Finsler metric will satisfy the requirements.

A.2 Proof of necessary conditions

Proposition 6 *The necessary conditions for a minimum in Eq. 6 is*

$$\begin{aligned} 2G(x_t)u_t + \mu_t &= 0, \quad t = 0, \dots, T-1, \\ x_{t+1} &= x_t + u_t, \quad t = 0, \dots, T-1, \\ \nabla_y \left[u_t^\top G(y)u_t \right] \Big|_{y=x_t} + \mu_t &= \mu_{t-1}, \quad t = 1, \dots, T-1. \\ x_0 &= a, x_T = b. \end{aligned} \tag{A1}$$

where $\mu_t \in \mathbb{R}^d$ for $t = 0, \dots, T-1$.

Proof The Hamiltonian of Eq. 6 is

$$H_t(x_t, u_t, \mu_t) = u_t^\top G(x_t)u_t + \mu_t^\top (x_t + u_t). \tag{A2}$$

The Hamiltonian $H_t(x_t, u_t, \mu_t)$ is strictly convex in u_t , since $G(x_t)$ is positive definite. The time-discrete version of Pontryagin's maximum principle [56] then yields the following when applied to our control problem (6)

$$\begin{aligned}
2G(x_t)u_t + \mu_t &= 0, \quad t = 0, \dots, T-1, \\
x_{t+1} &= x_t + u_t, \quad t = 0, \dots, T-1, \\
\nabla_y \left[u_t^\top G(y)u_t \right] \Big|_{y=x_t} + \mu_t &= \mu_{t-1}, \quad t = 1, \dots, T-1. \\
x_0 &= a, x_T = b.
\end{aligned} \tag{A3}$$

□

A.3 Proof of update scheme for Riemannian geometry

Proposition 7 *The update scheme in eq. 7 and eq. 9 for u_t, μ_t and x_t can in closed-form be written as*

$$\begin{aligned}
\mu_{T-1} &= \left(\sum_{t=0}^{T-1} G_t^{-1} \right)^{-1} \left(2(a-b) - \sum_{t=0}^{T-1} G_t^{-1} \sum_{t>j}^{T-1} \nu_j \right), \\
u_t &= -\frac{1}{2} G_t^{-1} \left(\mu_{T-1} + \sum_{j>t}^{T-1} \nu_j \right), \quad t = 0, \dots, T-1, \\
x_{t+1} &= x_t + u_t, \quad t = 0, \dots, T-1, \\
x_0 &= a.
\end{aligned}$$

Proof From the update formula $\nu_t + \mu_t = \mu_{t-1}$ for $t = 1, \dots, T-1$ we deduce that $\mu_t = \mu_{T-1} + \sum_{j>t}^{T-1} \nu_j$. From the update scheme $2G_t u_t + \mu_t = 0$ we deduce that $u_t = -\frac{1}{2} G_t^{-1} \mu_t$, since G_t is positive definite and hence has a well-defined inverse. Noting that $\sum_{t=0}^{T-1} u_t = b-a$ we can re-write the iterative formulas as

$$\begin{aligned}
\mu_t &= \mu_{T-1} + \sum_{j>t}^{T-1} \nu_j, \quad t = 0, \dots, T-1, \\
u_t &= -\frac{1}{2} G_t^{-1} \left(\mu_{T-1} + \sum_{j>t}^{T-1} \nu_j \right), \quad t = 0, \dots, T-1, \\
-\frac{1}{2} \sum_{t=0}^{T-1} G_t^{-1} \left(\mu_{T-1} + \sum_{j>t+1}^{T-1} \nu_j \right) &= b-a.
\end{aligned}$$

The last equation can be used to solve for μ_{T-1} utilizing that the sum of (inverse) positive definite matrices is positive definite and has a well-defined inverse

$$\mu_{T-1} = \left(\sum_{t=0}^{T-1} G_t^{-1} \right)^{-1} \left(2(a-b) - \sum_{t=0}^{T-1} G_t^{-1} \sum_{t>j}^{T-1} \nu_j \right),$$

which proves the result. □

A.4 Proof of update scheme for Finslerian geometry

Consider the following control problem in the Finslerian case.

$$\begin{aligned}
\min_{x_0:T} \quad & \sum_{t=0}^{T-1} u_t^\top G(x_t, u_t) u_t, \quad t = 0, \dots, T-1, \\
\text{s.t.} \quad & x_{t+1} = x_t + u_t \\
& x_0 = a, x_T = b,
\end{aligned} \tag{A4}$$

By similar computation as in Proposition. 1 with G is now dependent on both x_t and u_t , we get the following equation system to be solved in iteration $i + 1$ derived from Pontryagin's maximum principle by fixing variables

$$\begin{aligned}
\nu_t + \mu_t &= \mu_{t-1}, \quad t = 1, \dots, T-1, \\
2G_t u_t + \zeta_t + \mu_t &= 0, \quad t = 0, \dots, T-1, \\
\sum_{t=0}^{T-1} u_t &= b - a, \\
\nu_t &:= \nabla_y (u_t^\top G(y, u_t) u_t) \Big|_{y=x_t^{(i)}, u_t=u_t^{(i)}}, \quad t = 1, \dots, T-1, \\
\zeta_t &:= \nabla_y (u_t^\top G(x_t, y) u_t) \Big|_{x_t=x_t^{(i)}, u_t=u_t^{(i)}, y=u_t^{(i)}}, \quad t = 1, \dots, T-1, \\
G_t &:= G(x_t^{(i)}, u_t^{(i)}), \quad t = 0, \dots, T-1,
\end{aligned} \tag{A5}$$

The related state variables (before line search) are found by the state equation, $x_{t+1} = x_t + u_t$ for $t = 0, \dots, T-1$ with $x_0 = a$. Using the same approach as in the proof of Proposition 2, then Eq. A5 is equivalent to

$$\begin{aligned}
\mu_{T-1} &= \left(\sum_{t=0}^{T-1} G_t^{-1} \right)^{-1} \left(2(a-b) - \sum_{t=0}^{T-1} G_t^{-1} \left(\zeta_t + \sum_{t>j}^{T-1} \nu_j \right) \right), \\
u_t &= -\frac{1}{2} G_t^{-1} \left(\mu_{T-1} + \zeta_t + \sum_{j>t}^{T-1} \nu_j \right), \quad t = 0, \dots, T-1, \\
x_{t+1} &= x_t + u_t, \quad t = 0, \dots, T-1, \\
x_0 &= a,
\end{aligned} \tag{A6}$$

where it is exploited that the fundamental tensor is positive definite.

A.5 Proof of global convergence

To prove global convergence for the algorithm *GEORCE* we first show existence and uniqueness by proving two lemmas. Secondly, we prove that in each iteration the discretized energy functional is decreasing, unless a (local) minimum has been found. We will assume Lipschitz continuity of the metric tensor as described in 5.

For notation set $x^{(i)} = (a, x_1^{(i)}, \dots, x_{T-1}^{(i)}, b)$ and $u^{(i)} = (u_0^{(i)}, u_1^{(i)}, \dots, u_{T-2}^{(i)}, u_{T-1}^{(i)})$ as the solution for iteration i such that $(x^{(i+1)}, u^{(i+1)})$ is the solution using the update scheme in proposition 2. Let $\langle \cdot, \cdot \rangle$ denote the standard inner product in \mathbb{R}^n .

Lemma 8 *Assume that $(x^{(i)}, u^{(i)})$ is a feasible solution, then*

1. *There exists a unique solution $(x^{(i+1)}, u^{(i+1)})$ to the system of equations in eq. 10 based on $(x^{(i)}, u^{(i)})$.*
2. *All linear combinations $(1 - \alpha)(x^{(i)}, u^{(i)}) + \alpha(x^{(i+1)}, u^{(i+1)})$ for $0 < \alpha \leq 1$ are feasible solutions.*

Proof Since the matrices, $\{G(x_t^{(i)})\}_{t=0}^T$ are positive definite, then the matrices are regular with unique inverse, and so are the sum of the inverse matrices. This means that there exists an unique solution to the update scheme in proposition 2 proving 1.

Since the solution $(x^{(i+1)}, u^{(i+1)})$ is also a feasible solution for the update scheme in proposition 2, then the linear combination of two feasible solutions will also be a feasible solution, i.e.

$$\sum_{t=0}^{T-1} u_t^{(j)} = (b - a), \quad j = 1, \dots, (i + 1).$$

The new solution based on the linear combination gives

$$\begin{aligned} (1 - \alpha) \sum_{t=0}^{T-1} u_t^{(i)} + \alpha \sum_{t=0}^{T-1} u_t^{(i+1)} &= (1 - \alpha)(b - a) + \alpha(b - a) = (b - a) \\ (1 - \alpha)x^{(i)} + \alpha x^{(i+1)} &= (1 - \alpha)(\alpha, x_1^{(i)}, \dots, x_{T-1}^{(i)}, b) + \alpha(a, x_1^{(i+1)}, \dots, x_{T-1}^{(i+1)}, b) \\ &= (a, (1 - \alpha)x_1^{(i)} + \alpha x_1^{(i+1)}, \dots, (1 - \alpha)x_{T-1}^{(i)} + \alpha x_{T-1}^{(i+1)}, b), \end{aligned}$$

where for any $t = 0, \dots, T - 1$

$$\begin{aligned} (1 - \alpha)x_t^{(i)} + \alpha x_t^{(i+1)} &= (1 - \alpha) \left(a + \sum_{j=0}^{t-1} u_j^{(i)} \right) + \alpha \left(a + \sum_{j=0}^{t-1} u_j^{(i+1)} \right) \\ &= a + \sum_{j=0}^{t-1} \left((1 - \alpha)u_j^{(i)} + \alpha u_j^{(i+1)} \right). \end{aligned}$$

This shows that the linear combination in the state is feasible as it produces feasible state variables in terms of start and end point. Furthermore, each state variable is feasible, if they were determined from the linear combination of the control vectors, which proves that the linear combinations of the state and control variables are also feasible solutions. \square

Lemma 9 *Let $\{x_t^{(i)}, u_t^{(i)}\}_{t=0}^T$ denote the feasible solution after iteration i in GEORCE. If $\{x_t^{(i)}, u_t^{(i)}\}_{t=0}^T$ is not a (local) minimum point, then the feasible solution from iteration*

$\{x_t^{(i+1)}, u_t^{(i+1)}\}_{t=0}^T$ will decrease the objective function in the sense that there exists an $\eta > 0$ such that for all α with $0 < \alpha \leq \eta \leq 1$, then

$$E\left(x^{(i)} + \alpha\left(x^{(i+1)} - x^{(i)}\right), u^{(i)} + \alpha\left(u^{(i+1)} - u^{(i)}\right)\right) < E\left(x^{(i)}, u^{(i)}\right),$$

where $x^{(i)} = (a, x_1^{(i)}, \dots, x_{T-1}^{(i)}, b)$ and $u^{(i)} = (u_0^{(i)}, u_1^{(i)}, \dots, u_{T-2}^{(i)}, u_{T-1}^{(i)})$.

Proof $E(x, u)$ is a smooth function. The first order Taylor approximation of the energy function $E(x, u)$ in eq. 5 in (x, u) is

$$\begin{aligned} \Delta E(x, u) &= \sum_{t=1}^{T-1} \left(\left\langle \nabla_{x_t} E(x_t, u_t) \Big|_{(x_t, u_t) = (x_t^{(i)}, u_t^{(i)})}, \Delta x_t \right\rangle + \mathcal{O}(\Delta x_t) \|\Delta x_t\| \right) \\ &\quad + \sum_{t=0}^{T-1} \left(\left\langle \nabla_{u_t} E(x_t, u_t) \Big|_{(x_t, u_t) = (x_t^{(i)}, u_t^{(i)})}, \Delta u_t \right\rangle + \mathcal{O}(\Delta u_t) \|\Delta u_t\| \right), \end{aligned}$$

where $\Delta u_t := u_t^{(i+1)} - u_t^{(i)}$ and $\Delta x_t := x_t^{(i+1)} - x_t^{(i)}$. By the optimality conditions in eq. 7 we have that

$$\begin{aligned} \nabla_{x_t} E(x, u) \Big|_{(x, u) = (x_t^{(i)}, u_t^{(i)})} &= \mu_{t-1} - \mu_t, \quad t = 1, \dots, T-1, \\ \nabla_{u_t} E(x_t, u_t) \Big|_{(x_t, u_t) = (x_t^{(i)}, u_t^{(i+1)})} &= -\mu_t, \quad t = 0, \dots, T-1. \end{aligned} \tag{A7}$$

Inserting the optimality conditions in the Taylor expansion we have that

$$\begin{aligned} \Delta E(x, u) &= \sum_{t=1}^{T-1} (\langle \mu_{t-1} - \mu_t, \Delta x_t \rangle + \mathcal{O}(\Delta x_t) \|\Delta x_t\|) \\ &\quad + \sum_{t=0}^{T-1} \left(\left\langle \nabla_{u_t} E(x, u) \Big|_{(x, u) = (x_t^{(i)}, u_t^{(i)})}, \Delta u_t \right\rangle + \mathcal{O}(\Delta u_t) \|\Delta u_t\| \right). \end{aligned}$$

Since $\Delta x_t = \sum_{j=0}^{t-1} \Delta u_j$, then

$$\begin{aligned} \Delta E(x, u) &= \sum_{t=1}^{T-1} \left(\left\langle \mu_{t-1} - \mu_t, \sum_{j=0}^{t-1} \Delta u_j \right\rangle + \mathcal{O} \left(\sum_{j=0}^{t-1} \Delta u_j \right) \left\| \sum_{j=0}^{t-1} \Delta u_j \right\| \right) \\ &\quad + \sum_{t=0}^{T-1} \left(\left\langle \nabla_{u_t} E(x, u) \Big|_{(x, u) = (x_t^{(i)}, u_t^{(i)})}, \Delta u_t \right\rangle + \mathcal{O}(\Delta u_t) \|\Delta u_t\| \right). \end{aligned}$$

Re-arranging the terms we get

$$\begin{aligned}
\Delta E(x, u) &= \sum_{t=0}^{T-2} \left\langle \mu_t, \sum_{j=0}^t \Delta u_j \right\rangle \\
&\quad - \sum_{t=1}^{T-1} \left(\left\langle \mu_t, \sum_{j=0}^{t-1} \Delta u_j \right\rangle + \mathcal{O} \left(\sum_{j=0}^{t-1} \Delta u_j \right) \left\| \sum_{j=0}^{t-1} \Delta u_j \right\| \right) \\
&\quad + \sum_{t=0}^{T-1} \left(\left\langle \nabla_{u_t} E(x_t, u_t) \Big|_{(x_t, u_t) = (x_t^{(i)}, u_t^{(i)})}, \Delta u_t \right\rangle + \mathcal{O}(\Delta u_t) \|\Delta u_t\| \right) \\
&= \langle \mu_0, \Delta u_0 \rangle + \sum_{t=1}^{T-2} \langle \mu_t, \Delta u_t \rangle - \left\langle \mu_{T-1}, \sum_{j=0}^{T-1} \Delta u_j \right\rangle + \langle \mu_{T-1}, \Delta u_{T-1} \rangle \\
&\quad + \sum_{t=0}^{T-1} \left(\left\langle \nabla_{u_t} E(x_t, u_t) \Big|_{(x_t, u_t) = (x_t^{(i)}, u_t^{(i)})}, \Delta u_t \right\rangle + \mathcal{O}(\Delta u_t) \|\Delta u_t\| \right)
\end{aligned}$$

Since $\Delta u_j = u_j^{(i+1)} - u_j^{(i)}$ and $\Delta x_j = x_j^{(i+1)} - x_j^{(i)}$ for $j = 0, \dots, T$, and since the solution is feasible we have that $\sum_{j=0}^{T-1} u_j^{(i)} = b - a$ for any i , which implies that $\sum_{j=0}^{T-1} \Delta u_j = 0$. This reduces the above expression to

$$\begin{aligned}
\Delta E(x, u) &= \sum_{t=0}^{T-1} \left(\langle \mu_t, \Delta u_t \rangle + \mathcal{O} \left(\sum_{j=0}^{t-1} \Delta u_j \right) \left\| \sum_{j=0}^{t-1} \Delta u_j \right\| \right) \\
&\quad + \sum_{t=0}^{T-1} \left(\left\langle \nabla_{u_t} E(x_t, u_t) \Big|_{(x_t, u_t) = (x_t^{(i)}, u_t^{(i)})}, \Delta u_t \right\rangle + \mathcal{O}(\Delta u_t) \|\Delta u_t\| \right) \\
&= \sum_{t=0}^{T-1} \left\langle \mu_t + \nabla_{u_t} E(x, u) \Big|_{(x, u) = (x_t^{(i)}, u_t^{(i)})}, \Delta u_t \right\rangle \\
&\quad + \sum_{t=0}^{T-1} \mathcal{O} \left(\sum_{j=0}^{t-1} \Delta u_j \right) \left\| \sum_{j=0}^{t-1} \Delta u_j \right\| + \sum_{t=0}^{T-1} \mathcal{O}(\Delta u_t) \|\Delta u_t\|.
\end{aligned}$$

By eq. A7 we have

$$\begin{aligned}
\mu_t + \nabla_{u_t} E(x_t, u_t) \Big|_{(x_t, u_t) = (x_t^{(i)}, u_t^{(i)})} &= -\nabla_{u_t} E(x_t, u_t) \Big|_{(x_t, u_t) = (x_t^{(i)}, u_t^{(i+1)})} \\
&\quad + \nabla_{u_t} E(x, u) \Big|_{(x, u) = (x_t^{(i)}, u_t^{(i)})} \\
&= -2G(x_t^{(i)}) (u_t^{(i+1)} - u_t^{(i)}),
\end{aligned} \tag{A8}$$

which implies that

$$\begin{aligned}
\Delta E(x, u) &= \sum_{t=0}^{T-1} \left\langle -2G(x_t^{(i)}) \Delta u_t, \Delta u_t \right\rangle \\
&\quad + \sum_{t=0}^{T-1} \left(\mathcal{O} \left(\sum_{j=0}^{t-1} \Delta u_j \right) \left\| \sum_{j=0}^{t-1} \Delta u_j \right\| + \mathcal{O}(\Delta u_t) \|\Delta u_t\| \right).
\end{aligned} \tag{A9}$$

Since $G(x_t^{(i)})$ is positive definite, the first summation is negative assuming that at least one non-zero vector $\{\Delta u_t\}_{t=0}^{T-1}$, which is the case, since we have assumed that $(x_t^{(i)}, u_t^{(i)})$ is not

a (local) minimum. Now scale all vectors, $\{\Delta u_t\}_{t=0}^{T-1}$ with a scalar $0 < \alpha < 1$. Note that the term, $-2G(x_t^{(i)}) \Delta u_t$, is unaffected by this, since it equals $\mu_t + \nabla_{u_t} E(x, u)(x_t^{(i)}, u_t^{(i)})$, which is independent of α . The first order Taylor order approximation is

$$\begin{aligned} \Delta E(x, u) &= \sum_{t=0}^{T-1} \langle -2G(x_t^{(i)}) \Delta u_t, \alpha \Delta u_t \rangle \\ &\quad + \sum_{t=0}^{T-1} \left(\mathcal{O} \left(\sum_{j=0}^{t-1} \alpha \Delta u_j \right) \left\| \sum_{j=0}^{t-1} \alpha \Delta u_j \right\| + \mathcal{O}(\alpha \Delta u_t) \|\alpha \Delta u_t\| \right). \end{aligned}$$

In the limit it now follows that there exists an $\eta > 0$ such that $\frac{\Delta E(x, u)}{\alpha} < 0$ for some α with $0 < \alpha \leq \eta \leq 1$, which implies that $\Delta E(x, u) < 0$. \square

Theorem 10 *Let $E^{(i)}$ be the value of the discretized energy functional for the solution after iteration i (with line search) in GEORCE. If the starting point $(x^{(0)}, u^{(0)})$ is feasible, then the series $\{E^{(i)}\}_{i>0}$ will converge to a (local) minimum.*

Proof If the starting point $(x^{(0)}, u^{(0)})$ in GEORCE is feasible, then the points $(x^{(i)}, u^{(i)})$ after each iteration (with line-search) in GEORCE will also be feasible solutions by lemma 8.

The discretized energy functional is a positive function, i.e. a lower bound is at least 0. Assume that the series $\{E^{(i)}\}_{i>0}$ is not converging to a (local) minimum. From lemma 9 it follows that $\{E^{(i)}\}_{i>0}$ is decreasing for increasing i , and since $E^{(i)}$ has a lower bound, the series $\{E^{(i)}\}_i$ can not be non-converging. Assume now that the convergence value for $\{E^{(i)}\}_i$, denoted \hat{E} , is not a (local) minimum, and denote the convergence point (\hat{x}, \hat{u}) . According to lemma 9 GEORCE will from the solution (\hat{x}, \hat{u}) in the following iteration produce a new point (\tilde{x}, \tilde{u}) such that $E(\tilde{x}, \tilde{u}) < \hat{E}$, which is contradiction as the series $\{E^{(i)}\}_i$ is assumed to be converging to \hat{E} . The series, $\{E^{(i)}\}_i$, will therefore converge, and the convergence point is a (local) minimum. \square

Under the assumption of a strongly unique minimum point in Appendix A.1 GEORCE will converge to a local minimum by 3. Thus, it is not possible that GEORCE will "jump" between local minimas.

A.6 Proof of local quadratic convergence

In this section we show that GEORCE has locally quadratic convergence to a (local) minimum under certain assumptions satisfied by the discretized energy functional. We will assume the assumptions in 5 hold. We first prove the following result, before proving quadratic local convergence.

Lemma 11 *Assume $f(x)$ is a smooth function. Let z^* be a strongly unique (local) minimum point for f . Then*

$$\exists \epsilon > 0 : \quad \forall z \in B_\epsilon(z^*) \setminus \{z^*\} : \quad \langle \nabla f(z), z^* - z \rangle < 0.$$

Proof Since $f(x)$ is a smooth function, then the first order Taylor approximation for $f(x)$ exists. Consider a point $z \in B_\epsilon(z^*) \setminus \{z^*\}$, then

$$f(z^*) - f(z) = \langle \nabla f(z), z^* - z \rangle + \mathcal{O}(z^* - z) \|z^* - z\|.$$

Since z^* is a strongly unique (local) minimum point, then

$$f(z^*) - f(z) \leq -K \|z^* - z\| < 0, \quad K > 0,$$

which implies that

$$\frac{f(z^*) - f(z)}{\|z^* - z\|} = \left\langle \nabla f(z), \frac{z^* - z}{\|z^* - z\|} \right\rangle + \mathcal{O}(z^* - z) \leq -K.$$

Since $\lim_{z \rightarrow z^*} \mathcal{O}(z^* - z) = 0$, then there exists $\epsilon > 0$ such that

$$\left\langle \nabla f(z), \frac{z^* - z}{\|z^* - z\|} \right\rangle < 0,$$

which implies that $\langle \nabla f(z), z^* - z \rangle < 0$ for some $\epsilon > 0$ for all $z \in B_\epsilon(z^*) \setminus \{z^*\}$. \square

Proposition 12 *If the discretized energy functional has a strongly unique (local) minimum point z^* and locally $\alpha^* = 1$, i.e. no line search, then GEORCE has locally quadratic convergence, i.e.*

$$\exists \epsilon > 0 : \quad \exists c > 0 : \quad \forall z^{(i)} \in B_\epsilon(z^*) : \quad \|z^{(i+1)} - z^*\| \leq c \|z^{(i)} - z^*\|^2,$$

where $z^{(i)} = (x^{(i)}, u^{(i)})$ is the solution from GEORCE at iteration i .

Proof Assume that z^* is a (local) minimum point. Since GEORCE has global convergence to a (local) minimum point by theorem 3, we will assume that the algorithm has convergence point $E(z^*)$. Consider iteration i with $z^{(i)} = (x^{(i)}, u^{(i)})$ from GEORCE, and assume that all following iterations in GEORCE is in the ball $B_{\epsilon_1}(z^*)$, and fulfills the strongly unique assumption in 5. Note that as the series $\{z^{(i)}\}$ converge to z^* , then $\{z^{(i)}\}_{i>k} \subset B_{\epsilon_1}(z^*)$ for some $k > 0$. It then follows from the assumption of strongly unique minimizing point that for some $K > 0$

$$E(z^{(i+1)}) - E(z^*) \geq K \|z^{(i+1)} - z^*\|,$$

since $z^{(i+1)} \in B_{\epsilon_1}(z^*)$. The left hand term above can be rearranged into

$$E(z^{(i+1)}) - E(z^*) = \left(E(z^{(i+1)}) - E(z^{(i)}) \right) + \left(E(z^{(i)}) - E(z^*) \right).$$

By eq. A9 in the proof of lemma 9 and utilizing $\alpha^* = 1$, it follows that

$$\begin{aligned}
& E(z^{(i+1)}) - E(z^*) \\
&= \left(E(z^{(i+1)}) - E(z^{(i)}) \right) + \left(E(z^{(i)}) - E(z^*) \right) \\
&= \sum_{t=0}^{T-1} \left(\left\langle -2G(x_t^{(i)}) \Delta u_t, \Delta u_t \right\rangle + \mathcal{O} \left(\sum_{j=0}^{t-1} \Delta u_j \right) \left\| \sum_{j=0}^{t-1} \Delta u_j \right\| + \mathcal{O}(\Delta u_t) \|\Delta u_t\| \right) \\
&\quad - \sum_{t=0}^{T-1} \left\langle -2G(x_t^{(i)}) \Delta u_t, (u_t^* - u_t^{(i)}) \right\rangle \\
&\quad - \mathcal{O} \left(\sum_{j=0}^{t-1} (u_j^* - u_j^{(i)}) \right) \left\| \sum_{j=0}^{t-1} (u_j^* - u_j^{(i)}) \right\| - \mathcal{O}(u_t^* - u_t^{(i)}) \|u_t^* - u_t^{(i)}\| \\
&= \sum_{t=0}^{T-1} \left(\left\langle -2G(x_t^{(i)}) \Delta u_t, \Delta u_t - (u_t^* - u_t^{(i)}) \right\rangle + \mathcal{O} \left(\sum_{j=0}^{t-1} \Delta u_j \right) \left\| \sum_{j=0}^{t-1} \Delta u_j \right\| \right) \\
&\quad + \sum_{t=0}^{T-1} \left(\mathcal{O}(\Delta u_t) \|\Delta u_t\| + \mathcal{O} \left(\sum_{j=0}^{t-1} (u_j^* - u_j^{(i)}) \right) \left\| \sum_{j=0}^{t-1} (u_j^* - u_j^{(i)}) \right\| \right) \\
&\quad + \sum_{t=0}^{T-1} \left(\mathcal{O}(u_t^* - u_t^{(i)}) \|u_t^* - u_t^{(i)}\| \right) \\
&= \sum_{t=0}^{T-1} \left(\left\langle 2G(x_t^{(i)}) \Delta u_t, u_t^* - u_t^{(i+1)} \right\rangle + \mathcal{O} \left(\sum_{j=0}^{t-1} \Delta u_j \right) \left\| \sum_{j=0}^{t-1} \Delta u_j \right\| \right) \\
&\quad + \sum_{t=0}^{T-1} \mathcal{O}(\Delta u_t) \|\Delta u_t\| \\
&\quad + \sum_{t=0}^{T-1} \left(\mathcal{O} \left(\sum_{j=0}^{t-1} (u_j^* - u_j^{(i)}) \right) \left\| \sum_{j=0}^{t-1} (u_j^* - u_j^{(i)}) \right\| + \mathcal{O}(u_t^* - u_t^{(i)}) \|u_t^* - u_t^{(i)}\| \right).
\end{aligned}$$

Observe now that the term $2G(x_t^{(i)}) \Delta u_t$ is the gradient for $z_t^{(i)}$. Define ϵ_2 such that the \mathcal{O} -terms are sufficiently close to zero for all $z \in B_{\epsilon_2}(z^*)$. Thus, for $\epsilon = \min\{\epsilon_1, \epsilon_2\}$ we have from lemma 11

$$\sum_{t=0}^{T-1} \left\langle 2G(x_t^{(i)}) \Delta u_t, u_t^* - u_t^{(i+1)} \right\rangle < 0,$$

since z^* is assumed to be a strongly unique minimum point by assumptions 5. Combining the inequalities and utilizing that $E(z)$ is locally Lipschitz continuous by assumptions 5, then

$$K \|z^{(i+1)} - z^*\| \leq E(z^{(i+1)}) - E(z^*) \leq \mathcal{O} \left(\|z^i - z^*\|^2 \right),$$

which implies that there exists an $\epsilon > 0$ such that

$$\forall z^{(i)} \in B_\epsilon(z^*) : \|z^{(i+1)} - z^*\| \leq c \|z^{(i)} - z^*\|^2,$$

for $c > 0$. □

The assumption in the above proof that the line search parameter, $\alpha^* = 1$ locally at the minimum point is based on that locally the approximation of the discretized energy functional becomes close to the true function.

A.7 Extension to Finslerian manifolds

The proof for global convergence and local quadratic convergence hold similar for *GEORCE* in the Finsler case. Let E_F denote the corresponding discretized Finsler energy functional. For the Finsler case the optimality condition becomes

$$\begin{aligned} \nabla_{x_t} E_F(x_t, u_{t0}) \Big|_{(x_t, u_t) = (x_t^{(i)}, u_t^{(i)})} &= \mu_{T-1} - \mu_t, \quad t = 1, \dots, T-1, \\ \nabla_{u_t} E_F(x_t, u_t) \Big|_{(x_t, u_t) = (x_t^{(i)}, u_t^{(i+1)})} &= 2G(x_t^{(i)}, u_t^{(i)}) u_t^{(i+1)} + \zeta_t = -\mu_t, \\ &t = 0, \dots, T-1 \end{aligned} \quad (\text{A10})$$

The proof of global and local quadratic convergence are completely similar for the Riemannian and Finsler case except that eq. A8 in the Finsler case becomes

$$\begin{aligned} \mu_t + \nabla_{u_t} E_F(x_t, u_t) \Big|_{(x_t, u_t) = (x_t^{(i)}, u_t^{(i)})} &= -\nabla_{u_t} E_F(x_t, u_t) \Big|_{(x_t, u_t) = (x_t^{(i+1)}, u_t^{(i+1)})} \\ &+ \nabla_{u_t} E_F(x_t, u_t) \Big|_{(x_t, u_t) = (x_t^{(i+1)}, u_t^{(i)})} \\ &= -\left(G(x_t^{(i)}, u_t^{(i)}) u_t^{(i+1)} + \zeta_t \right) \\ &+ \left(2G(x_t^{(i)}, u_t^{(i)}) + \zeta_t \right) \\ &= -2G(x_t^{(i)}, u_t^{(i)}) \left(u_t^{(i+1)} - u_t^{(i)} \right), \end{aligned} \quad (\text{A11})$$

by using the properties of *GEORCE* in the Finsler case in eq. A10. Eq. A11 is completely similar to eq. A8 in the Riemannian case, and from that the global convergence and local quadratic convergence proofs are completely similar to the Riemannian case.

Appendix B Algorithms

B.1 GEORCE for Finsler manifolds

In Algorithm 2 we show *GEORCE* for Finsler manifolds in pseudo-code using the update scheme in Eq. 14.

B.2 Sparse Newton Method

In this section we derive a sparse Newton method for minimizing eq. 5. We consider the Riemannian case, but note that it is easily generalized to the Finslerian case. The

Algorithm 2 GEORCE for Finsler Manifolds

- 1: **Input:** tol, T
- 2: **Output:** Geodesic estimate $x_{0:T}$
- 3: Set $x_t^{(0)} \leftarrow a + \frac{b-a}{T}t$, $u_t^{(0)} \leftarrow \frac{b-a}{T}$ for $t = 0, \dots, T$ and $i \leftarrow 0$
- 4: **while do** $\left\| \nabla_y E(y) \Big|_{y=x_t^{(i)}} \right\|_2 > \text{tol}$
- 5: $G_t \leftarrow G \left(x_t^{(i)}, u_t^{(i)} \right)$ for $t = 0, \dots, T-1$
- 6: $\nu_t \leftarrow \nabla_y \left(u_t^{(i)} G \left(y, u_t^{(i)} \right) u_t^{(i)} \right) \Big|_{y=x_t^{(i)}}$ for $t = 1, \dots, T-1$
- 7: $\zeta_t \leftarrow \nabla_y \left(u_t^{(i)} G \left(x_t^{(i)}, y \right) u_t^{(i)} \right) \Big|_{y=u_t^{(i)}}$ for $t = 1, \dots, T-1$
- 8: $\mu_{T-1} \leftarrow \left(\sum_{t=0}^{T-1} G_t^{-1} \right)^{-1} \left(2(a-b) - \sum_{t=0}^{T-1} G_t^{-1} \left(\zeta_t + \sum_{t>j}^{T-1} \nu_j \right) \right)$
- 9: $u_t \leftarrow -\frac{1}{2} G_t^{-1} \left(\mu_{T-1} + \zeta_t + \sum_{j>t}^{T-1} \nu_j \right)$ for $t = 0, \dots, T-1$
- 10: $x_{t+1} \leftarrow x_t + u_t$ for $t = 0, \dots, T-1$
- 11: Using line search find α^* for the following optimization problem with the discrete energy functional E_F

$$\begin{aligned} \alpha^* &= \arg \min_{\alpha} E_F(x_{0:T}) \quad (\text{exact line-search}) \\ \text{s.t.} \quad &x_{t+1} = x_t + \alpha u_t + (1-\alpha)u_t^{(i)}, \quad t = 0, \dots, T-1, \\ &x_0 = a. \end{aligned}$$

- 12: Set $u_t^{(i+1)} \leftarrow \alpha^* u_t + (1-\alpha^*)u_t^{(i)}$ for $t = 0, \dots, T-1$
 - 13: Set $x_{t+1}^{(i+1)} \leftarrow x_t^{(i+1)} + u_t^{(i+1)}$ for $t = 0, \dots, T-1$
 - 14: $i \leftarrow i+1$
 - 15: **end while**
 - 16: return x_t for $t = 0, \dots, T-1$
-

Hessian of the eq. 5 we get that

$$\begin{aligned} \partial_{x_t x_t}^2 E(x_{0:T}) &= \partial_{x_t x_t}^2 u_t^\top G(x_t) u_t \Big|_{u_t=x_{t+1}-x_t} + 2G(x_{t-1}) - 2G(x_t) \\ &\quad + 4\nabla_{x_{t-1}} G(x_{t-1}) u_t \Big|_{u_t=x_t-x_{t-1}} - 4\nabla_{x_t} G(x_t) u_t \Big|_{u_t=x_{t+1}-x_t}, \quad t = 1, \dots, T-1, \\ \partial_{x_t x_{t+1}}^2 E(x_{0:T}) &= 2\nabla_{x_t} G(x_t) u_t \Big|_{u_t=x_{t+1}-x_t}, \quad t = 1, \dots, T-2, \\ \partial_{x_{t+1} x_t}^2 E(x_{0:T}) &= 2(G(x_t) u_t)^\top \Big|_{u_t=x_{t+1}-x_t}, \quad t = 1, \dots, T-2. \end{aligned}$$

where ∂_{x_i, x_j}^2 denotes the second order derivative. From this we see that the Hessian can be written as

$$H = \begin{pmatrix} H_{11} & H_{12} & 0 & 0 & 0 & 0 & 0 & \dots & 0 \\ H_{21} & H_{22} & H_{23} & 0 & 0 & 0 & 0 & \dots & 0 \\ 0 & H_{23} & H_{33} & H_{34} & 0 & 0 & 0 & \dots & 0 \\ 0 & 0 & H_{43} & H_{33} & H_{45} & 0 & 0 & \dots & 0 \\ 0 & 0 & 0 & H_{54} & H_{55} & H_{56} & 0 & \dots & 0 \\ 0 & 0 & 0 & 0 & H_{65} & H_{66} & H_{67} & \dots & 0 \\ \vdots & \ddots & \vdots \\ 0 & 0 & 0 & 0 & 0 & 0 & \dots & H_{(T-2)(T-2)} & H_{(T-1)(T-2)} \\ 0 & 0 & 0 & 0 & 0 & 0 & \dots & H_{(T-2)(T-1)} & H_{(T-1)(T-1)} \end{pmatrix}, \quad (\text{B12})$$

where we define

$$H_{ij} = \partial_{x_i, x_j}^2 E(x_{0:T}),$$

A Newton step has the following form at iteration j .

$$s^{(j)} = -H^{-1} \nabla_{x_{1:(T-1)}} E(x_{0:T}), \quad (\text{B13})$$

To simplify notation, define $s_i := -\nabla_{x_i} E(x_{0:T})$. Using the block structure in eq. B12, we can recursively solve eq. B13 similar to the Thomas Algorithm [57].

$$\begin{aligned} s_i &\leftarrow H_{ii}^{-1} s_i, \\ P &\leftarrow H_{ii+1}^\top, \quad i+1 < T \\ H_{ii+1} &\leftarrow H_{ii}^{-1} H_{ii+1}, \quad i+1 < T \\ H_{i+1, i+1} &\leftarrow H_{i+1, i+1} - H_{i+1, i} H_{i, i+1} = H_{i+1, i+1} - P H_{i, i+1}, \quad i+1 < T \\ s_{i+1} &\leftarrow s_{i+1} - H_{i+1, i} s_i = s_{i+1} - P s_i, \quad i+1 < T. \end{aligned} \quad (\text{B14})$$

such that the Newton step is updated for $i = T-2, \dots, 1$

$$s_i \leftarrow s_i - H_{i, i+1} s_{i+1}. \quad (\text{B15})$$

Note that we efficiently solve the equations in eq. B14 as

$$\begin{aligned} H_{ii} y_i &= (H_{ii+1} | s_i), \quad i = 1, \dots, T-2, \\ H_{T-1} y_{T-1} &= s_{T-1}, \end{aligned} \quad (\text{B16})$$

such that only one linear system of equations has to be solved in each iteration. The Newton method does not have global convergence. In Algorithm 3 we write the Sparse Newton algorithm in pseudo-code switching between the Newton method and gradient descent with line-search. Note that the above is easily extended to the Finslerian case, where G denotes the fundamental tensor and depends on both x and u . Note that the sparse Newton algorithm in Algorithm 3 has complexity $\mathcal{O}(Td^3)$ completely similar to GEORCE.

Algorithm 3 Sparse Newton Method

1: **Input:** tol, T
2: **Output:** Geodesic estimate $x_{0:T}$
3: Set $x_t^{(0)} \leftarrow a + \frac{b-a}{T}t$ for $t = 0, \dots, T$ and $j \leftarrow 0$
4: **while do** $\left\| \nabla_y E(y) \Big|_{y=x_t^{(i)}} \right\|_2 > \text{tol}$
5: Compute $\left\{ s_t^{\text{grad}}, s_t^{\text{newton}} \right\}_{t=1, \dots, T-2}$ using eq. B14 and eq. B15.
6: **if then** $\sum_{t=1}^{T-1} s_t^{\text{grad}} (s_t^{\text{newton}})^\top \geq 0$
7: $s_t = s_t^{\text{newton}}$ for $t = 1, \dots, T-1$
8: **else**
9: $s_t = s_t^{\text{grad}}$ for $t = 1, \dots, T-1$
10: **end if**
11: Perform line-search for $\alpha^* = \arg \min_{0 \leq \alpha \leq 1} E(x_{1:(T-1)} + \alpha s_{1:(T-1)})$ with
12:
$$x_t^{(j+1)} \leftarrow x_t^{(j)} + \alpha^* s_t, \quad t = 1, \dots, T-1.$$

13: $j \leftarrow j + 1$
14: **end while**
15: return $x_t^{(j)}$ for $t = 0, \dots, T-1$

Since the Hessian of the energy is not necessarily positive definite, the Newton scheme can be numerically unstable. To avoid this, we represent in Algorithm 4 a regularized Newton method by adding suitable scaling in the diagonal. Note that the Newton method for the discretized energy was also proposed in [58], which also formulates the Hessian as a block matrix similar to eq. B12. However, they do not derive an adaptive scheme to solve the linear equation in the Newton step or propose the regularized version in Algorithm 4.

Appendix C Manifolds

Table C1 contains a description of the Riemannian manifolds shown in the paper.

In the Finsler cases we consider a Riemannian manifold with a background metric, G , equipped with a force-field.

$$f(x) = \frac{\sin x \odot \cos x}{(\cos x)^\top G(x) \cos x},$$

where x denotes the local coordinates of the manifold. In this case the corresponding metric is a Randers metric, which is a special case of Riemannian metrics, of the form [51]

Algorithm 4 Sparse Regularized Newton Method

```

1: Input: tol,  $T$ ,  $\lambda$ ,  $\kappa$ 
2:
3: Output: Geodesic estimate  $x_{0:T}$ 
4:
5: Set  $x_t^{(0)} \leftarrow a + \frac{b-a}{T}t$  for  $t = 0, \dots, T$  and  $j \leftarrow 0$ 
6:
7: while do  $\left\| \nabla_y E(y) \Big|_{y=x_t^{(j)}} \right\|_2 > \text{tol}$ 
8:    $H_{ii} \leftarrow \lambda I + \partial_{x_i x_i}^2 E(x_{0:T})$ 
9:
10:   $H_{ij} \leftarrow \partial_{x_i x_j}^2 E(x_{0:T})$ 
11:
12:  Compute  $\{s_t^{\text{grad}}, s_t^{\text{newton}}\}_{t=1, \dots, T-2}$  using eq. B14 and eq. B15.
13:
14:  if then  $\sum_{t=1}^{T-1} s_t^{\text{grad}} (s_t^{\text{newton}})^\top \geq 0$ 
15:
16:     $s_t = s_t^{\text{newton}}$  for  $t = 1, \dots, T-1$ 
17:
18:     $\lambda \leftarrow \kappa \lambda$ 
19:  else
20:     $s_t = s_t^{\text{grad}}$  for  $t = 1, \dots, T-1$ 
21:
22:     $\lambda \leftarrow \lambda / \kappa$ 
23:  end if
24:  Perform line-search for  $\alpha^* = \arg \min_{0 \leq \alpha \leq 1} E(x_{1:(T-1)} + \alpha s_{1:(T-1)})$  with
      
$$x_t^{(j+1)} \leftarrow x_t^{(j)} + \alpha^* s_t, \quad t = 1, \dots, T-1.$$

25:   $j \leftarrow j + 1$ 
26: end while
27: return  $x_t^{(j)}$  for  $t = 0, \dots, T-1$ 

```

$$\begin{aligned}
 F &= \sqrt{a_{ij} \dot{r}^i \dot{r}^j} + b_i \dot{r}^i \\
 a_{ij} &= g_{ij} \lambda + f_i f_j \lambda^2 \\
 b_i &= -f_i \lambda \\
 f_i &= g_{ij} f^j \\
 \lambda^{-1} &= v_0^2 - g_{ij} f^i f^j,
 \end{aligned} \tag{C17}$$

where g_{ij} denotes the elements of the Riemannian background metric, f^j denotes the j th element of the force field, while v_0 denotes the initial velocity Riemannian

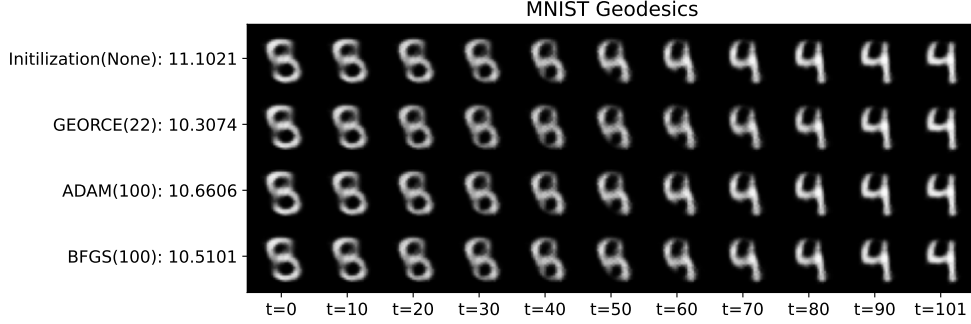


Fig. D1 The figure shows the results of using *GEORCE* and alternative methods for constructing geodesics for a Variational-Autoencoder [52] (VAE) for the MNIST dataset [54]. All algorithms are terminated if the ℓ^2 -norm of the gradient of the discretized energy functional in eq. 5 is less than 10^{-3} , or if the number of iterations exceeds 100. We see that *GEORCE* uses less iterations and obtains the smallest length compared to the other algorithms. The details of the manifolds and experiments can be found in the supplementary material.

length of an object moving with constant velocity v on the surface. For the manifold to be a proper Finsler manifold it is required that $\|f\|_g < v_0$.

Appendix D Variational autoencoders

D.1 Architecture

We train a Variational-Autoencoder (VAE) [52], where we use the normal distribution as a variational family to approximate the data distribution. We train a VAE for each of the following datasets

- MNIST data [54]: The data consists of 28×28 images of handwritten digits between 0 and 9. The data consists of 60,000 training images and 10,000 testing images.
- SVHN data [55]: The data consists of $32 \times 32 \times 3$ images of house numbers obtained through Google street view. The data consists of 73,257 digits for training and 26,032 digits for testing. We use approximately 80% of the training data for training similar to [12].
- CelebA data [53]: The data consists of 202,599 images of famous people of size $64 \times 64 \times 3$, where we use approximately 80% for training similar to [12].

The architectures for the VAE for MNIST data, SVHN data and CelebA data are shown in Table D2, Table D3 and Table D4, respectively. The architecture is similar to [12] with some modifications. All models are trained for 50,000 epochs on a GPU described in Appendix E.2.

D.2 Additional experiments

In Fig. D1 and Fig. D2 we show the geodesics between two reconstructed images using the learned VAE for the MNIST VAE and SVHN VAE, respectively, where we show the results using *GEORCE*, the initialization and alternative methods.

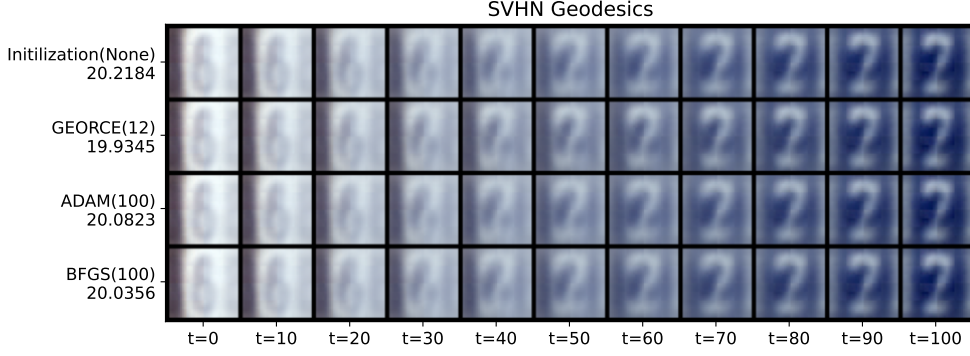


Fig. D2 The figure shows the results of using *GEORCE* and alternative methods for constructing geodesics for a Variational-Autoencoder [52] (VAE) for the SVHN dataset [55]. All algorithms are terminated if the ℓ^2 -norm of the gradient of the discretized energy functional in eq. 5 is less than 10^{-3} , or if the number of iterations exceeds 100. We see that *GEORCE* uses less iterations and obtains the smallest length compared to the other algorithms. The details of the manifolds and experiments can be found in the supplementary material.

Appendix E Experiments

The following contains details of hyper-parameters, hardware and additional experiments. The implementation and code can be found at <https://github.com/FrederikMR/georce>.

E.1 Hyper-parameters and methods

Table E5 shows the hyper parameters used for the different methods. It is the same hyper-parameters that have been used for all manifolds across dimension and grid size in the paper.

Table E6 shows the integration methods used for solving the shooting problem.

All the timing estimates are computed by compiling the algorithms first, and then running the algorithm five times to compute the mean and standard deviation of the runtime. Table E7 states the start and end point of the geodesics constructed on the different manifolds in a local coordinate system as described in Table C1.

E.2 Hardware

All figures have been computed on a *HP* computer with Intel Core i9-11950H 2.6 GHz 8C, 15.6" FHD, 720P CAM, 32 GB (2×16GB) DDR4 3200 So-Dimm, Nvidia Quadro TI2004GB Descrete Graphics, 1TB PCIe NVMe SSD, backlit Keyboard, 150W PSU, 8cell, W11Home 64 Advanced, 4YR Onsite NBD.

The runtime experiments on a CPU have been run on a CPU model *XeonE5-2660v3* with 4 nodes for at most 24 hours with a maximum memory of 10 GB. .

The runtime estimates on a GPU and training of the VAE have been computed on a GPU for at most 24 hours with a maximum memory of 10 GB. The *GPU* consists of 4 nodes on a *Tesla V100*.

E.3 Additional experiments

In the following we show run time estimates computed similar to the description in the main paper with other methods than *BFGS* and *ADAM*. It should be noted that a gradient method with exact line search has also been tested against *GEORCE*, but shows similar computational behavior as *ADAM*, but often with higher computational times and therefore not included in the following. We also show the results on a GPU for CUDA compatible methods.

Note that for the Finsler manifold for the ellipsoid of dimension 50 with a grid size of $T = 50$ points, none of the methods converge including *GEORCE*. This is due to the strong variation by the force field causing numerical instability. However, when the grid size is increased to $T = 100$, *GEORCE* converges to the best solution across all algorithms indicating that it requires a finer grid for this example.

E.4 Run-Time Estimates on VAE Manifolds

We show in Table E8 the run-time estimates on learned manifolds using a VAE.

E.4.1 Additional Run-time estimates on a GPU

We show in Table E9 and Table E10 the runtime of GPU compatible methods for different Riemannian manifolds, and in Table E11 and Table E12 the runtime of GPU compatible methods for different Finsler manifolds.

E.4.2 Additional Run-time estimates on a CPU

Methods on a Riemannian manifold

We show in Table E13, Table E14, Table E15, Table E16, Table E17, Table E18, Table E19 and Table E20 runtime estimates for different methods on a CPU for the different Riemannian manifolds.

Methods on a Finsler manifold

We show in Table E21, Table E22, Table E23, Table E24, Table E25, Table E26, Table E27 and Table E28 runtime estimates for different methods on a CPU for different Finsler manifolds.

Manifold	Description	Parameters	Local Coordinates
\mathbb{S}^n	The n-sphere, $\{x \in \mathbb{R}^{n+1} \mid \ x\ _2 = 1\}$	-	Stereographic coordinates
$E(n)$	The n-Ellipsoid, $\{x \in \mathbb{R}^{n+1} \mid \ p \odot x\ _2 = 1\}$	Half-axes: $p = (0.5, \dots, 1)$ equally distributed points.	Stereographic coordinates
\mathbb{T}^2	Torus	Major radius $R = 3.0$ and minor radius $r = 1.0$	Parameterized by (θ, ϕ) with $x = (R + r \cos \theta) \cos \phi, y = (R + r \cos \theta) \sin \phi, z = r \sin \theta$.
\mathbb{H}^2	2 dimensional Hyperbolic Space embedded into Minkowski space \mathbb{R}^3	-	Parameterized by (α, β) with $x = \cosh \alpha, y = \sinh \alpha \cos \beta, z = \sinh \alpha \sin \beta$.
$\mathcal{P}(n)$	Paraboloid of dimension n	-	Parameterized by standard coordinates by $(x^1, \dots, x^n, \sum_{i=1}^n x_i^2)$
$\mathcal{P}(n)$	Symmetric positive definite matrices of size n^2	-	Embedded into \mathbb{R}^{n^2} by the mapping $f(x) = l(x)l(x)^T$, where $l : \mathbb{R}^{n(n+1)/2} \rightarrow \mathbb{R}^{n \times n}$ maps x into a lower triangle matrix consisting of the elements in x .
'Egg-tray'	A parameterized surface in shape of an egg tray	-	Parameterized by (x, y) with $x = x, y = y, z = 2 \cos x \cos y$.
Gaussian Distribution	Parameters of the Gaussian distribution equipped with the Fischer-Rao metric	-	Parameterized by $(\mu, \sigma) \in \mathbb{R} \times \mathbb{R}_+$.
Fréchet Distribution	Parameters of the Fréchet distribution equipped with the Fischer-Rao metric	-	Parameterized by $(\beta, \lambda) \in \mathbb{R}_+ \times \mathbb{R}_+$.
Cauchy Distribution	Parameters of the Cauchy distribution equipped with the Fischer-Rao metric	-	Parameterized by $(\mu, \sigma) \in \mathbb{R} \times \mathbb{R}_+$.
Pareto Distribution	Parameters of the Pareto distribution equipped with the Fischer-Rao metric	-	Parameterized by $(\theta, \alpha) \in \mathbb{R}_+ \times \mathbb{R}_+$.
VAE MNIST	Variational-Autoencoder equipped with the pull-back metric for MNIST-data	-	Parameterized by the encoded latent space.
VAE SVHN	Variational-Autoencoder equipped with the pull-back metric for SVHN-data	-	Parameterized by the encoded latent space.
VAE CelebA	Variational-Autoencoder equipped with the pull-back metric for CelebA-data	-	Parameterized by the encoded latent space.

Table C1 Description of the manifolds used in the paper.

Encoder	
Conv (output_channels = 64, kernel_shape = 4 × 4, stride = 2, bias = False)	GELU
Conv (output_channels = 64, kernel_shape = 4 × 4, stride = 2, bias = False)	GELU
Conv (output_channels = 64, kernel_shape = 4 × 4, stride = 1, bias = False)	GELU
Conv (output_channels = 64, kernel_shape = 4 × 4, stride = 2, bias = False)	GELU
Latent Parameters	
μ : Linear(out_feature = 8, bias = True), Identity	
σ : Linear(out_feature = 8, bias = True), Sigmoid	
Decoder	
Linear (out_feature = 50, bias = True)	GELU
Conv2dTransposed (output_channels = 64, kernel_shape = 4 × 4, stride = 2, bias = False)	GELU
Conv2dTransposed (output_channels = 32, kernel_shape = 4 × 4, stride = 1, bias = False)	GELU
Conv2dTransposed (output_channels = 16, kernel_shape = 4 × 4, stride = 1, bias = False)	GELU
Linear (out_feature = 784, bias = True)	

Table D2 Architecture for VAE for the MNIST-dataset

Encoder	
Conv (output_channels = 32, kernel_shape = 2 × 2, stride = 2, bias = False)	GELU
Conv (output_channels = 32, kernel_shape = 2 × 2, stride = 2, bias = False)	GELU
Conv (output_channels = 64, kernel_shape = 2 × 2, stride = 2, bias = False)	GELU
Conv (output_channels = 64, kernel_shape = 2 × 2, stride = 2, bias = False)	GELU
Latent Parameters	
μ : Linear(out_feature = 32, bias = True), Identity	
σ : Linear(out_feature = 32, bias = True), Sigmoid	
Decoder	
Conv2dTransposed (output_channels = 64, kernel_shape = 2 × 2, stride = 2, bias = False)	GELU
Conv2dTransposed (output_channels = 64, kernel_shape = 2 × 2, stride = 2, bias = False)	GELU
Conv2dTransposed (output_channels = 32, kernel_shape = 2 × 2, stride = 2, bias = False)	GELU
Conv2dTransposed (output_channels = 32, kernel_shape = 2 × 2, stride = 2, bias = False)	GELU
Conv2dTransposed (output_channels = 3, kernel_shape = 2 × 2, stride = 2, bias = False)	

Table D3 Architecture for VAE for the SVHN-dataset

Encoder	
Conv (output_channels = 32, kernel_shape = 4 × 4, stride = 2, bias = False)	
GELU	
Conv (output_channels = 32, kernel_shape = 4 × 4, stride = 2, bias = False)	
GELU	
Conv (output_channels = 64, kernel_shape = 4 × 4, stride = 2, bias = False)	
GELU	
Conv (output_channels = 64, kernel_shape = 4 × 4, stride = 2, bias = False)	
GELU	
Latent Parameters	
μ : Linear(out_feature = 32, bias = True), Identity	
σ : Linear(out_feature = 32, bias = True), Sigmoid	
Decoder	
Conv2dTransposed (output_channels = 64, kernel_shape = 4 × 4, stride = 2, bias = False)	
GELU	
Conv2dTransposed (output_channels = 64, kernel_shape = 4 × 4, stride = 2, bias = False)	
GELU	
Conv2dTransposed (output_channels = 32, kernel_shape = 4 × 4, stride = 2, bias = False)	
GELU	
Conv2dTransposed (output_channels = 32, kernel_shape = 4 × 4, stride = 2, bias = False)	
GELU	
Conv2dTransposed (output_channels = 3, kernel_shape = 4 × 4, stride = 4, bias = False)	

Table D4 Architecture for VAE for the CelebA-dataset

Method	Description	Parameters
<i>GEORCE</i>	See algorithm in main paper	Backtracking: $\rho = 0.5$.
<i>ADAM</i> [41]	Moments based gradient descent method	$\gamma = 0.01$ (step size), $\beta_1 = 0.9$, $\beta_2 = 0.999$, $\epsilon = 10^{-8}$
<i>SGD</i> [59]	Stochastic gradient descent	$\gamma = 0.01$ (step size), momentum=0, dampening=0, weight_decay=0.
<i>BFGS</i> [37–40]	Quasi-Newton method	-
<i>CG</i> [60]	Conjugate-Gradient method	-
<i>dogleg</i> [60]	trust region algorithm	-
<i>trust_ncg</i> [60]	Newton conjugate trust-region algorithm	-
<i>trust_exact</i> [60]	nearly exact trust region algorithm	-
<i>Sparse Newton</i>	See Appendix B.2	Backtracking: $\rho = 0.5$.
<i>Sparse Regularized Newton</i>	See Appendix B.2	Backtracking: $\rho = 0.5$ with $\lambda = 1.0$ and $\kappa = 0.5$.

Table E5 The Hyper-parameters for estimating of the geodesics. We refer to Scipy [61] for the description and implementation of *BFGS*, *CG*, *dogleg*, *trust_ncg* and *trust_exact*.

Method	Description	Parameters
<i>RK45</i> [62]	The explicit Runge-Kutta of order four to five	-
<i>RK23</i> [63]	The explicit Runge-Kutta of order two to three	-
<i>DOP853</i> [64]	The explicit Runge-Kutta of order eight	-
<i>Radau</i> [65]	Implicit Runge-Kutta method using Radau method	-
<i>BDF</i> [66]	Implicit multi-step order using backward differentiation	-
<i>LSODA</i> [67]	Method combining BDF and ADAM with stiffness detection	-

Table E6 The ODE methods. The descriptions are from the *Scipy*-library [61].

Manifold	Start point	End point
\mathbb{S}^n	n equally spaced points between 0 and 1 (end point is excluded)	$(0.5, 0.5, \dots, 0.5)$
$E(n)$	n equally spaced points between 0 and 1 (end point is excluded)	$(0.5, 0.5, \dots, 0.5)$
\mathbb{T}^2	$(0.0, 0.0)$	$(5\pi/4, 5\pi/4)$
\mathbb{H}^2	$(1.0, 1.0)$	$(0.1, 0.1)$
Paraboloid	$(1, 1)$	$(0, 0.5)$
$\mathcal{P}(n)$	The identity matrix in local coordinates	$n(n + 1)/2$ equally spaced points between 0.5 and 1.0.
'Egg-tray'	$(-5.0, 5.0)$	$(5.0, 5.0)$
Gaussian Distribution	$(\mu_0, \sigma_0) = (-1.0, 0.5)$	$(\mu_T, \sigma_T) = (1.0, 1.0)$
Fréchet Distribution	$(\beta_0, \lambda_0) = (0.5, 0.5)$	$(\beta_T, \lambda_T) = (1.0, 1.0)$
Cauchy Distribution	$(\mu_0, \sigma_0) = (-1.0, 0.5)$	$(\mu_T, \sigma_T) = (1.0, 1.0)$
Pareto Distribution	$(\theta_0, \alpha_0) = (0.5, 0.5)$	$(\theta_T, \alpha_T) = (1.0, 1.0)$

Table E7 The start and end point for the geodesics estimated for each manifold.

Riemannian Manifold	BFGS (T=100)		ADAM (T=100)		GEORCE (T=100)	
	Length	Runtime	Length	Runtime	Length	Runtime
VAE MNIST	10.3075	1407.5743 ± 6.4430	10.3312	645.5201 ± 2.6648	10.3074	67.6149 ± 0.0304
VAE SVHN	—	—	19.9855	13325.2285 ± 123.4978	19.9346	882.4120 ± 1.8839
VAE CelebA	—	—	—	—	42.2666	2222.5259 ± 8.2988

Table E8 The table shows the length of the estimated geodesics for the *BFGS*-algorithm, *ADAM* and *GEORCE* on a CPU. The methods were terminated if the ℓ^2 -norm of the gradient was less than 10^{-3} or 1,000 iterations have been reached. When the computational time was longer than 24 hour, the value is set to —.

Riemannian Manifold	ADAM (T=100)		Sparse Newton (T=100)		GEORCE (T=100)	
	Length	Runtime	Length	Runtime	Length	Runtime
S^2	2.2755	0.2729 ± 0.0016	2.2742	0.1417 ± 0.0041	2.2741	0.0163 ± 0.0003
S^3	2.4376	0.2890 ± 0.0005	2.4342	0.2188 ± 0.0039	2.4342	0.0735 ± 0.0018
S^5	2.4226	0.3153 ± 0.0027	2.3755	0.8657 ± 0.0015	2.3755	0.0494 ± 0.0014
S^{10}	2.1031	0.3052 ± 0.0079	1.9653	117.4589 ± 0.0140	1.9523	0.0351 ± 0.0001
S^{20}	1.6824	0.3401 ± 0.0117	1.7069	146.3024 ± 0.0191	1.4808	0.0483 ± 0.0020
S^{50}	1.1456	0.5339 ± 0.0014	1.0359	310.2160 ± 0.0200	0.9749	0.0587 ± 0.0023
S^{100}	0.8475	1.2935 ± 0.0014	0.7522	6.6464 ± 0.0016	0.4188	0.0717 ± 0.0022
S^{250}	0.6251	3.8386 ± 0.0018	0.4958	98.6502 ± 0.0147	0.3192	0.3296 ± 0.0005
S^{500}	0.5714	8.2031 ± 0.0030	0.3787	899.4549 ± 0.0188	0.2198	1.2925 ± 0.0003
S^{1000}	0.5270	19.2234 ± 0.0712	—	—	0.1573	6.8579 ± 0.0023
E (3)	1.9595	0.2735 ± 0.0074	1.9595	0.2177 ± 0.0075	1.9595	0.0138 ± 0.0001
E (5)	2.0523	0.2839 ± 0.0056	2.0498	0.3705 ± 0.0063	2.0501	0.0167 ± 0.0001
E (10)	1.9594	0.2948 ± 0.0116	—	—	1.8410	0.0827 ± 0.0036
E (20)	1.6421	0.3097 ± 0.0133	1.4247	116.6572 ± 0.0186	1.5139	0.0547 ± 0.0019
E (50)	1.3052	0.3875 ± 0.0058	1.4583	148.6781 ± 0.0307	0.6514	0.1449 ± 0.0054
E (100)	0.9245	0.5704 ± 0.0013	0.8849	316.9808 ± 0.0179	0.4642	0.0370 ± 0.0014
E (250)	0.6873	1.3063 ± 0.0020	0.5922	5.2868 ± 0.0007	0.3249	0.0524 ± 0.0002
E (500)	0.4974	4.2084 ± 0.0029	0.3917	84.6331 ± 0.0439	0.2180	0.2325 ± 0.0001
E (1000)	0.4559	7.4772 ± 0.0024	0.3039	827.7163 ± 0.1003	0.1468	1.2897 ± 0.0004
\mathbb{T}^2	0.4238	19.8033 ± 0.0970	—	—	0.1129	5.1862 ± 0.0071
\mathbb{H}^2	9.9853	0.2890 ± 0.0016	9.9851	0.3353 ± 0.0126	9.9851	0.0549 ± 0.0010
\mathcal{P} (2)	1.2500	0.3201 ± 0.0004	1.2498	0.2125 ± 0.0128	1.2498	0.0089 ± 0.0003
\mathcal{P} (3)	1.0786	0.3801 ± 0.0047	1.0669	0.2419 ± 0.0069	1.0669	0.0227 ± 0.0010
Gaussian Distribution	2.3006	0.4115 ± 0.0009	2.3810	106.2814 ± 0.0135	2.2639	0.0343 ± 0.0004
Fréchet Distribution	2.5951	0.1809 ± 0.0010	2.5952	0.1108 ± 0.0055	2.5952	0.0123 ± 0.0002
Cauchy Distribution	1.1538	0.1778 ± 0.0029	1.1539	0.0813 ± 0.0044	1.1539	0.0055 ± 0.0003
Pareto Distribution	1.6452	0.1818 ± 0.0007	1.6453	0.1136 ± 0.0067	1.6452	0.0137 ± 0.0001
	0.8314	0.1779 ± 0.0026	0.8297	0.0758 ± 0.0036	0.8297	0.0043 ± 0.0002

Table E9 The table shows the length of the estimated geodesics for different methods on a GPU. The methods have been stopped if the norm of the gradient was less than 10^{-4} or if a maximum of 1,000 iterations has been reached. When the computational time was longer than 24 hours, the value is set to —.

Riemannian Manifold	ADAM (T=50)		Sparse Newton (T=50)		GEORCE (T=50)	
	Length	Runtime	Length	Runtime	Length	Runtime
S^2	2.2479	0.2683 ± 0.0082	2.2478	0.1094 ± 0.0047	2.2477	0.0187 ± 0.0002
S^3	2.4069	0.2593 ± 0.0110	2.4064	0.1370 ± 0.0082	2.4064	0.0866 ± 0.0031
S^5	2.3494	0.2907 ± 0.0103	2.3480	0.3153 ± 0.0063	2.3480	0.0622 ± 0.0019
S^{10}	1.9470	0.3026 ± 0.0014	1.9274	0.8966 ± 0.0034	1.9272	0.0540 ± 0.0016
S^{20}	1.5036	0.3349 ± 0.0069	1.4610	28.7634 ± 0.0016	1.4566	0.0670 ± 0.0003
S^{50}	1.0320	0.4713 ± 0.0025	1.0060	39.8257 ± 0.0010	0.5279	0.0438 ± 0.0002
S^{100}	0.7642	0.8173 ± 0.0009	0.6922	4.2461 ± 0.0007	0.3932	0.0704 ± 0.0027
S^{250}	0.5136	3.2362 ± 0.0009	0.4589	60.6258 ± 0.0179	0.2748	0.1525 ± 0.0002
S^{500}	0.4253	7.7012 ± 0.0038	0.3278	706.9603 ± 0.0293	0.1858	0.7340 ± 0.0006
S^{1000}	0.3790	20.5850 ± 0.0098	—	—	0.1626	3.1229 ± 0.0007
E (2)	1.9331	0.2723 ± 0.0013	1.9330	0.1365 ± 0.0083	1.9331	0.0155 ± 0.0003
E (3)	2.0243	0.2852 ± 0.0017	2.0233	0.1828 ± 0.0074	2.0235	0.0305 ± 0.0012
E (5)	1.8262	0.2996 ± 0.0079	1.8047	0.6859 ± 0.0047	1.8054	0.1172 ± 0.0050
E (10)	1.5193	0.3094 ± 0.0086	0.9472	57.6302 ± 0.0107	1.4788	0.0855 ± 0.0036
E (20)	1.2028	0.3379 ± 0.0049	0.7603	48.7781 ± 0.0029	1.1366	0.0727 ± 0.0033
E (50)	0.8382	0.4596 ± 0.0092	0.6157	153.9548 ± 0.0165	0.4417	0.0284 ± 0.0001
E (100)	0.6175	0.8219 ± 0.0036	0.5822	3.9507 ± 0.0014	0.3160	0.0373 ± 0.0001
E (250)	0.4216	2.4940 ± 0.0028	0.3882	48.5547 ± 0.0120	0.2039	0.1519 ± 0.0003
E (500)	0.3454	5.5967 ± 0.0145	—	—	0.1434	0.7326 ± 0.0005
E (1000)	0.3056	14.1006 ± 0.0361	—	—	0.0996	4.1512 ± 0.0043
T^2	9.8952	0.2821 ± 0.0029	9.8943	38.0816 ± 0.0018	9.8955	0.0531 ± 0.0013
\mathbb{H}^2	1.2435	0.3072 ± 0.0003	1.2434	0.1172 ± 0.0048	1.2434	0.0082 ± 0.0001
\mathcal{P} (2)	1.0704	0.3571 ± 0.0072	1.0567	0.1231 ± 0.0051	1.0567	0.0243 ± 0.0002
\mathcal{P} (3)	2.2400	0.3924 ± 0.0057	2.3328	57.1278 ± 0.0125	2.2304	0.0198 ± 0.0001
Gaussian Distribution	2.5779	0.1785 ± 0.0003	2.5778	0.0617 ± 0.0027	2.5778	0.0130 ± 0.0002
Fréchet Distribution	1.1471	0.1696 ± 0.0004	1.1457	0.0442 ± 0.0016	1.1457	0.0063 ± 0.0002
Cauchy Distribution	1.6341	0.0230 ± 0.0002	1.6340	0.0810 ± 0.0037	1.6340	0.0135 ± 0.0003
Pareto Distribution	0.8235	0.0357 ± 0.0003	0.8235	0.0439 ± 0.0014	0.8234	0.0052 ± 0.0003

Table E10 The table shows the length of the estimated geodesics for different methods on a GPU. The methods have been stopped if the norm of the gradient was less than 10^{-4} or if a maximum of 1,000 iterations has been reached. When the computational time was longer than 24 hours, the value is set to —.

Finsler Manifold	ADAM ($T=100$)		Sparse Newton ($T=100$)		GEORCE ($T=100$)	
	Length	Runtime	Length	Runtime	Length	Runtime
S^2	1.6530	0.7706 ± 0.0018	1.6525	0.2512 ± 0.0089	1.6525	0.0372 ± 0.0004
S^3	1.7451	0.7362 ± 0.0036	—	—	1.7432	0.0431 ± 0.0005
S^5	1.7371	0.9292 ± 0.0038	—	—	1.7029	0.1036 ± 0.0048
S^{10}	1.5174	1.1358 ± 0.0018	1.4783	208.1472 ± 0.0176	1.4109	0.1000 ± 0.0033
S^{20}	1.2009	1.5876 ± 0.0028	—	—	1.0760	0.1509 ± 0.0058
S^{50}	0.8130	2.0381 ± 0.0026	—	—	0.7283	0.1373 ± 0.0032
S^{100}	0.6146	2.7712 ± 0.0032	0.6210	972.0195 ± 0.0307	0.2553	0.1106 ± 0.0028
S^{250}	0.5196	3.9803 ± 0.0019	—	—	0.1636	0.5069 ± 0.0003
S^{500}	0.4849	6.6164 ± 0.0023	—	—	0.1417	1.6591 ± 0.0004
S^{1000}	0.3835	25.4638 ± 0.1448	—	—	0.1134	7.9991 ± 0.0074
E (2)	1.3634	0.7758 ± 0.0036	1.3616	0.3735 ± 0.0010	1.3618	0.0282 ± 0.0009
E (3)	1.4085	0.7541 ± 0.0032	—	—	1.4023	0.1273 ± 0.0047
E (5)	1.3305	1.0252 ± 0.0017	1.5359	170.9661 ± 0.0296	1.2956	0.1135 ± 0.0039
E (10)	1.1235	1.1254 ± 0.0045	—	—	1.0804	0.0825 ± 0.0031
E (20)	0.8987	1.6039 ± 0.0035	—	—	0.8121	0.1282 ± 0.0054
E (50)	0.6332	2.0424 ± 0.0034	—	—	0.2845	0.0770 ± 0.0004
E (100)	0.4953	2.6704 ± 0.0031	0.4577	470.9805 ± 0.1448	0.2018	0.1127 ± 0.0023
E (250)	0.4179	4.0843 ± 0.0009	—	—	0.1287	0.5239 ± 0.0047
E (500)	0.4139	6.9391 ± 0.0073	0.2580	1435.3881 ± 0.0832	0.0968	1.7109 ± 0.0010
E (1000)	0.3442	25.9660 ± 0.1038	—	—	0.0798	7.9988 ± 0.0079
\mathbb{T}^2	7.4054	0.8017 ± 0.0045	9.1903	152.0036 ± 0.0158	6.8067	0.3145 ± 0.0050
\mathbb{H}^2	1.3341	0.7949 ± 0.0072	1.3338	0.4562 ± 0.0004	1.3337	0.0256 ± 0.0006
\mathcal{P} (2)	0.7334	0.9344 ± 0.0013	0.7291	0.4309 ± 0.0014	0.7292	0.0286 ± 0.0005
\mathcal{P} (3)	1.2987	1.0812 ± 0.0006	1.2856	0.6885 ± 0.0009	1.2856	0.0365 ± 0.0005
Gaussian Distribution	1.6879	0.4962 ± 0.0034	1.6878	0.4148 ± 0.0055	1.6878	0.0255 ± 0.0004
Fréchet Distribution	0.5406	0.2307 ± 0.0069	0.5405	0.2060 ± 0.0042	0.5405	0.0088 ± 0.0003
Cauchy Distribution	1.1140	0.4994 ± 0.0017	1.1133	0.5167 ± 0.0042	1.1133	0.0367 ± 0.0017
Pareto Distribution	0.3885	0.1014 ± 0.0038	0.3884	0.1042 ± 0.0031	0.3883	0.0096 ± 0.0004

Table E11 The table shows the length of the estimated geodesics for different methods on a GPU. The methods have been stopped if the norm of the gradient was less than 10^{-4} or if a maximum of 1,000 iterations has been reached. When the computational time was longer than 24 hours, the value is set to —.

Finsler Manifold	ADAM ($T=50$)		Sparse Newton ($T=50$)		GEORCE ($T=50$)	
	Length	Runtime	Length	Runtime	Length	Runtime
S^2	1.6383	0.7833 ± 0.0056	1.6385	0.2064 ± 0.0073	1.6385	0.0457 ± 0.0004
S^3	1.7300	0.7587 ± 0.0049	—	—	1.7297	0.0499 ± 0.0003
S^5	1.6875	0.9909 ± 0.0022	—	—	1.6868	0.1432 ± 0.0050
S^{10}	1.4013	1.1472 ± 0.0024	—	—	1.3908	0.1747 ± 0.0067
S^{20}	1.0829	1.5583 ± 0.0016	—	—	1.0560	0.2663 ± 0.0005
S^{50}	0.7427	1.4442 ± 0.0038	—	—	0.3508	0.0594 ± 0.0003
S^{100}	0.5511	2.5558 ± 0.0020	—	—	0.2626	0.0850 ± 0.0024
S^{250}	0.4094	3.8872 ± 0.0020	—	—	0.1686	0.2660 ± 0.0042
S^{500}	0.3531	7.5214 ± 0.0022	0.2861	1388.8278 ± 0.0965	0.1193	1.1879 ± 0.0003
S^{1000}	0.3269	13.1209 ± 0.0379	—	—	0.0828	6.0238 ± 0.0039
E (2)	1.3460	0.1327 ± 0.0060	1.3460	0.2847 ± 0.0043	1.3461	0.0332 ± 0.0011
E (3)	1.3870	0.7621 ± 0.0034	—	—	1.3826	0.2156 ± 0.0006
E (5)	1.2780	0.9718 ± 0.0022	—	—	1.2757	0.1654 ± 0.0050
E (10)	1.0665	1.1072 ± 0.0025	—	—	1.0126	0.2215 ± 0.0062
E (20)	0.8405	1.5702 ± 0.0031	—	—	0.7946	0.1937 ± 0.0061
E (50)	0.5797	1.4336 ± 0.0029	—	—	—	—
E (100)	0.4334	2.0750 ± 0.0026	—	—	0.2046	0.0830 ± 0.0004
E (250)	0.3234	2.8610 ± 0.0021	—	—	0.1365	0.2644 ± 0.0029
E (500)	0.2862	5.1735 ± 0.0122	0.2428	905.0696 ± 0.0365	0.0940	0.9444 ± 0.0011
E (1000)	0.2723	10.4951 ± 0.0347	—	—	0.0893	4.4688 ± 0.0060
\mathbb{H}^2	7.2683	0.7530 \pm 0.0015	9.0475	78.7132 ± 0.0222	9.0475	13.7393 ± 0.0093
\mathcal{P} (2)	1.3328	0.7454 ± 0.0052	1.3316	0.2303 ± 0.0058	1.3316	0.0317 \pm 0.0003
\mathcal{P} (3)	0.7249	0.5927 ± 0.0008	0.7249	0.2189 ± 0.0051	0.7249	0.0331 \pm 0.0011
	1.2710	1.0184 ± 0.0008	1.2707	0.4325 ± 0.0020	1.2707	0.0434 \pm 0.0006
Gaussian Distribution	1.6796	0.4337 ± 0.0111	1.6806	0.2081 ± 0.0047	1.6806	0.0282 \pm 0.0017
Fréchet Distribution	0.5370	0.0829 ± 0.0032	0.5370	0.1059 ± 0.0042	0.5370	0.0111 \pm 0.0003
Cauchy Distribution	1.1085	0.0626 ± 0.0010	1.1084	0.2270 ± 0.0081	1.1084	0.0410 \pm 0.0015
Pareto Distribution	0.3857	0.0752 ± 0.0025	0.3856	0.1054 ± 0.0028	0.3857	0.0082 \pm 0.0003

Table E12 The table shows the length of the estimated geodesics for different methods on a GPU. The methods have been stopped if the norm of the gradient was less than 10^{-4} or if a maximum of 1,000 iterations has been reached. When the computational time was longer than 24 hours, the value is set to —.

Riemannian Manifold	BFGS (T=100)			ADAM (T=100)			GEORCE (T=100)		
	Length	Runtime		Length	Runtime		Length	Runtime	
S^2	2.2742	57.4164 ± 0.0616		2.2772	0.2335 ± 0.0005		2.2741	0.0078	± 0.0000
S^3	2.4342	67.4657 ± 0.4874		2.4377	0.3475 ± 0.0010		2.4342	0.0635	± 0.0001
S^5	2.3757	77.6975 ± 0.0741		2.4222	1.9894 ± 0.0188		2.3755	0.2219	± 0.0001
S^{10}	1.9529	150.0621 ± 0.8919		2.1016	4.4208 ± 0.0308		1.9523	0.3184	± 0.0002
S^{20}	1.4810	1068.8645 ± 17.2001		1.6839	8.7097 ± 0.0352		1.4808	0.6732	± 0.0204
S^{50}	1.0464	7350.6001 ± 244.3737		1.1463	61.8926 ± 0.3034		0.9749	4.1016	± 0.0201
S^{100}	—	—		0.8466	277.4217 ± 0.2280		0.4187	10.9208	± 0.0071
S^{250}	—	—		0.6244	1424.9031 ± 22.1592		0.3192	78.2937	± 0.0991
S^{500}	—	—		0.5717	2242.4697 ± 17.9769		0.2198	224.2761	± 0.4894
S^{1000}	—	—		0.5279	4329.6621 ± 38.0163		0.1573	893.4682	± 7.3130
E (2)	1.9595	56.9650 ± 0.4106		1.9596	0.2328 ± 0.0001		1.9595	0.0067	± 0.0001
E (3)	2.0499	94.1769 ± 0.7044		2.0525	0.3392 ± 0.0024		2.0501	0.0119	± 0.0000
E (5)	1.8403	194.5403 ± 1.3293		1.9521	2.2227 ± 0.0186		1.8410	0.4220	± 0.0038
E (10)	1.5114	427.6278 ± 4.1044		1.6384	4.5697 ± 0.0541		1.5139	0.4566	± 0.0016
E (20)	1.1795	1669.2692 ± 10.2877		1.3049	9.4335 ± 0.0507		0.6548	1.9786	± 0.0031
E (50)	0.8338	10685.6133 ± 321.6447		0.9244	73.5682 ± 0.3306		0.4642	2.4208	± 0.0222
E (100)	—	—		0.6872	289.4196 ± 2.5224		0.3249	7.7128	± 0.0714
E (250)	—	—		0.4978	1620.6428 ± 16.9546		0.2178	56.8527	± 0.1526
E (500)	—	—		0.4559	2135.6899 ± 30.5699		0.1467	220.1656	± 0.9902
E (1000)	—	—		0.4232	4398.9453 ± 25.8738		0.1131	641.7199	± 20.9901
\mathbb{T}^2	9.9851	92.7400 ± 3.1267		9.9855	0.1060 ± 0.0002		9.9851	0.0182	± 0.0003
\mathbb{H}^2	1.2499	75.0079 ± 0.1710		1.2499	0.0988 ± 0.0001		1.2498	0.0025	± 0.0001
\mathcal{P} (2)	1.0669	88.2739 ± 0.4152		1.0879	0.2611 ± 0.0004		1.0669	0.0141	± 0.0001
\mathcal{P} (3)	2.2639	168.5082 ± 0.3039		2.2896	2.3780 ± 0.0046		2.2639	0.1442	± 0.0002
Gaussian Distribution	2.5952	47.6288 ± 0.1359		2.5956	0.0167 ± 0.0001		2.5952	0.0015	± 0.0000
Fréchet Distribution	1.1538	51.3063 ± 0.0566		1.1542	0.0185 ± 0.0001		1.1539	0.0009	± 0.0000
Cauchy Distribution	1.6454	36.5031 ± 0.0437		1.6466	0.0177 ± 0.0001		1.6452	0.0020	± 0.0000
Pareto Distribution	0.8297	39.0465 ± 0.0471		0.8336	0.0168 ± 0.0000		0.8297	0.0007	± 0.0000

Table E13 The table shows the length of the estimated geodesics for different methods on a CPU. The methods have been stopped if the norm of the gradient was less than 10^{-4} or if a maximum of 1,000 iterations has been reached. When the computational time was longer than 24 hours, the value is set to —.

Riemannian Manifold	BFGS ($T=50$)		ADAM ($T=50$)		GEORGE ($T=50$)	
	Length	Runtime	Length	Runtime	Length	Runtime
S^2	2.2478	34.0090 ± 0.7480	2.2479	0.0996 ± 0.0000	2.2477	0.0048 ± 0.0000
S^3	2.4064	33.7983 ± 0.2472	2.4069	0.1720 ± 0.0001	2.4064	0.0408 ± 0.0000
S^5	2.3480	42.4323 ± 0.4287	2.3489	1.0908 ± 0.0111	2.3480	0.1484 ± 0.0001
S^{10}	1.9288	62.2979 ± 0.5799	1.9469	2.3366 ± 0.0018	1.9272	0.2462 ± 0.0015
S^{20}	1.4614	161.7671 ± 0.3882	1.5037	4.3590 ± 0.0024	1.4566	0.5572 ± 0.0009
S^{50}	0.9934	1028.2557 ± 1.4276	1.0320	34.7336 ± 0.1530	0.5279	1.6104 ± 0.0016
S^{100}	0.7500	4076.6101 ± 188.1693	0.7642	142.7405 ± 0.5381	0.3932	6.4462 ± 0.0468
S^{250}	—	—	0.5136	1163.6172 ± 5.2656	0.2748	25.8527 ± 0.0436
S^{500}	—	—	0.4253	2272.3826 ± 44.3587	0.1858	117.6824 ± 0.2510
S^{1000}	—	—	0.3790	4507.5815 ± 11.6850	0.1626	333.4426 ± 3.6572
$E(2)$	1.9330	38.1118 ± 0.0767	1.9337	0.0986 ± 0.0001	1.9331	0.0038 ± 0.0000
$E(3)$	2.0233	41.8059 ± 0.0366	2.0237	0.1594 ± 0.0056	2.0235	0.0110 ± 0.0000
$E(5)$	1.8045	140.1273 ± 1.0396	1.8262	1.0991 ± 0.0024	1.8054	0.3319 ± 0.0007
$E(10)$	1.4760	187.4378 ± 1.0853	1.5193	2.2661 ± 0.0032	1.4788	0.3963 ± 0.0019
$E(20)$	1.1489	329.3681 ± 2.5049	1.2029	3.8156 ± 0.0185	1.1366	0.4997 ± 0.0015
$E(50)$	0.7913	1755.3668 ± 3.7051	0.8382	34.8794 ± 0.1429	0.4417	1.0645 ± 0.0041
$E(100)$	0.5923	6260.6895 ± 30.3624	0.6175	144.6669 ± 1.0968	0.3160	3.4531 ± 0.0102
$E(250)$	—	—	0.4216	871.3954 ± 0.6870	0.2039	25.3168 ± 0.0372
$E(500)$	—	—	0.3454	1695.4600 ± 10.5103	0.1434	114.6093 ± 0.4502
$E(1000)$	—	—	0.3056	3026.5793 ± 37.3366	0.0996	429.9206 ± 0.2607
T^2	9.8955	59.2719 ± 0.3871	9.8950	0.0539 ± 0.0000	9.8955	0.0116 ± 0.0001
\mathbb{H}^2	1.2434	37.3124 ± 0.0360	1.2434	0.0439 ± 0.0002	1.2434	0.0014 ± 0.0000
$\mathcal{P}(2)$	1.0567	43.7359 ± 0.0490	1.0610	0.1343 ± 0.0015	1.0567	0.0081 ± 0.0002
$\mathcal{P}(3)$	2.2304	98.5211 ± 0.6390	2.2307	1.1962 ± 0.0194	2.2304	0.0500 ± 0.0001
Gaussian Distribution	2.5778	23.5395 ± 0.0607	2.5769	0.0084 ± 0.0001	2.5778	0.0011 ± 0.0000
Fréchet Distribution	1.1457	26.5810 ± 0.1445	1.1457	0.0097 ± 0.0001	1.1457	0.0006 ± 0.0000
Cauchy Distribution	1.6341	20.1153 ± 0.0478	1.6341	0.0012 ± 0.0000	1.6340	0.0012 ± 0.0000
Pareto Distribution	0.8235	22.4667 ± 0.0646	0.8235	0.0088 ± 0.0000	0.8234	0.0004 ± 0.0000

Table E14 The table shows the length of the estimated geodesics for different methods on a CPU. The methods have been stopped if the norm of the gradient was less than 10^{-4} or if a maximum of 1,000 iterations has been reached. When the computational time was longer than 24 hours, the value is set to —.

Riemannian Manifold	SGD ($T=100$)			CG ($T=100$)			dogleg ($T=100$)		
	Length	Runtime		Length	Runtime		Length	Runtime	
S^2	2.4063	0.2238 \pm 0.0075		2.2744	193.4884 \pm 2.7955		2.2742	3.8305 \pm 0.0143	
S^3	2.7102	0.3350 \pm 0.0007		2.4346	248.6363 \pm 2.7041		2.4342	5.6319 \pm 0.0156	
S^5	3.0827	2.1406 \pm 0.0095		2.3810	217.8721 \pm 4.5710		3.1069	1.7988 \pm 0.0217	
S^{10}	3.4578	4.6462 \pm 0.0732		1.9747	178.0182 \pm 0.0418		3.5092	6.9953 \pm 0.0104	
S^{20}	3.5726	8.8376 \pm 0.0048		1.4961	205.9335 \pm 1.9411		3.6632	41.3160 \pm 0.0809	
S^{50}	3.2831	72.7622 \pm 0.0207		1.2180	81.5957 \pm 0.0459		—	—	
S^{100}	2.8231	298.8796 \pm 0.0082		1.0540	109.8878 \pm 0.4428		—	—	
S^{250}	2.0949	2608.4075 \pm 40.8368		0.8580	391.9100 \pm 0.9132		—	—	
S^{500}	1.5779	10754.5576 \pm 300.1625		1.0325	709.8522 \pm 4.6273		—	—	
S^{1000}	—	—		1.1545	68.2710 \pm 0.7146		—	—	
E (2)	1.9693	0.2259 \pm 0.0018		1.9598	159.7566 \pm 1.6439		1.9595	3.9798 \pm 0.0834	
E (3)	2.0769	0.3266 \pm 0.0029		2.0504	269.9406 \pm 1.5354		2.0795	1.2249 \pm 0.0080	
E (5)	2.2219	2.2046 \pm 0.0154		1.8503	516.0936 \pm 11.2331		2.2269	1.7201 \pm 0.0152	
E (10)	2.4040	4.5520 \pm 0.0117		1.5794	286.3407 \pm 2.5997		2.4153	7.0164 \pm 0.0183	
E (20)	2.4961	8.8872 \pm 0.0029		1.1925	305.8136 \pm 2.2537		2.5175	40.8913 \pm 0.1881	
E (50)	2.3587	73.9033 \pm 0.2967		0.8949	181.0294 \pm 2.8838		—	—	
E (100)	2.0627	292.5031 \pm 1.1563		0.8718	177.2222 \pm 0.6547		—	—	
E (250)	1.5510	2521.6353 \pm 22.3619		0.8962	341.6886 \pm 1.5827		—	—	
E (500)	1.1756	10801.0918 \pm 301.4005		0.7106	1545.6230 \pm 10.8368		—	—	
E (1000)	—	—		0.8633	71.7434 \pm 0.1687		—	—	
\mathbb{T}^2	11.3048	0.1001 \pm 0.0000		9.9854	609.3215 \pm 9.3287		11.6903	1.2105 \pm 0.0095	
\mathbb{H}^2	1.3308	0.0839 \pm 0.0000		1.2532	549.9518 \pm 3.2561		1.2498	4.1077 \pm 0.0109	
\mathcal{P} (2)	1.1512	0.2608 \pm 0.0021		1.0676	420.3352 \pm 1.1349		1.0669	4.5709 \pm 0.0106	
\mathcal{P} (3)	2.3892	2.1047 \pm 0.0039		2.2648	570.4799 \pm 5.5919		2.4047	2.3496 \pm 0.0109	
Gaussian Distribution	2.8543	0.0115 \pm 0.0001		2.5955	374.0846 \pm 7.3067		2.5952	3.5420 \pm 0.0317	
Fréchet Distribution	1.1823	0.0134 \pm 0.0000		1.1547	321.4810 \pm 1.0877		1.1539	2.7293 \pm 0.0160	
Cauchy Distribution	1.9752	0.0119 \pm 0.0001		1.6461	192.8583 \pm 1.3344		1.6452	3.7594 \pm 0.0544	
Pareto Distribution	0.8500	0.0111 \pm 0.0001		0.8299	87.2695 \pm 0.1665		0.8297	2.2831 \pm 0.0390	

Table E15 The table shows the length of the estimated geodesics for different methods on a CPU. The methods have been stopped if the norm of the gradient was less than 10^{-4} or if a maximum of 1,000 iterations has been reached. When the computational time was longer than 24 hours, the value is set to —.

Riemannian Manifold	SGD ($T=50$)		CG ($T=50$)		dogleg ($T=50$)	
	Length	Runtime	Length	Runtime	Length	Runtime
S^2	2.3607	0.0963 \pm 0.0000	2.2478	112.6833 \pm 0.0636	2.2478	3.6126 \pm 0.0092
S^3	2.6515	0.1450 \pm 0.0005	2.4065	119.3687 \pm 0.3268	2.4064	4.7996 \pm 0.0220
S^5	2.9958	1.0907 \pm 0.0047	2.3483	132.6204 \pm 0.7172	3.0849	1.1818 \pm 0.0089
S^{10}	3.3093	2.2309 \pm 0.0017	1.9287	131.0700 \pm 2.7469	3.4892	2.2054 \pm 0.0121
S^{20}	3.3585	4.3963 \pm 0.0043	1.4644	197.9373 \pm 3.1216	3.6466	10.9397 \pm 0.0310
S^{50}	3.0604	33.8548 \pm 0.0592	1.0403	66.8326 \pm 0.4691	—	—
S^{100}	2.6628	142.5886 \pm 0.5246	0.8374	71.4308 \pm 0.1749	—	—
S^{250}	2.0317	1351.8007 \pm 6.9661	0.7906	151.2937 \pm 0.2754	—	—
S^{500}	1.5557	5792.4668 \pm 19.3864	0.9376	245.6238 \pm 1.3281	—	—
S^{1000}	—	—	0.8765	587.6923 \pm 4.5177	—	—
$E(2)$	1.9493	0.0959 \pm 0.0001	1.9331	91.2580 \pm 0.7684	1.9330	3.6286 \pm 0.0089
$E(3)$	2.0568	0.1565 \pm 0.0004	2.0234	188.5732 \pm 1.4986	2.0661	1.0738 \pm 0.0245
$E(5)$	2.1983	1.0906 \pm 0.0026	1.8099	319.5569 \pm 2.8321	2.2150	1.1382 \pm 0.0093
$E(10)$	2.3647	2.2644 \pm 0.0033	1.4779	364.8791 \pm 3.5348	2.4045	2.2572 \pm 0.0141
$E(20)$	2.4309	4.5347 \pm 0.0025	1.1536	256.8932 \pm 2.5821	2.5079	11.0630 \pm 0.0303
$E(50)$	2.2709	29.4273 \pm 0.1562	0.8494	99.0591 \pm 0.7024	—	—
$E(100)$	1.9914	123.1176 \pm 0.7069	0.6421	104.5576 \pm 0.4612	—	—
$E(250)$	1.5207	1334.2307 \pm 3.4387	0.6019	199.9802 \pm 0.7304	—	—
$E(500)$	1.1643	5472.2515 \pm 84.0089	0.6644	534.2835 \pm 2.8548	—	—
$E(1000)$	—	—	0.7192	640.3465 \pm 1.6748	—	—
T^2	10.5379	0.0498 \pm 0.0001	9.8956	239.9891 \pm 0.9619	11.5938	1.0782 \pm 0.0071
\mathbb{H}^2	1.3210	0.0425 \pm 0.0000	1.2434	367.4767 \pm 2.7398	1.2434	3.6867 \pm 0.0105
$\mathcal{P}(2)$	1.1238	0.1225 \pm 0.0009	1.0567	222.3136 \pm 1.0460	1.0567	3.6711 \pm 0.0168
$\mathcal{P}(3)$	2.3231	1.2252 \pm 0.0004	2.2306	364.5162 \pm 0.9199	2.3721	1.3057 \pm 0.0108
Gaussian Distribution	2.7366	0.0055 \pm 0.0001	2.5780	130.6218 \pm 0.8519	2.5778	3.4534 \pm 0.0148
Fréchet Distribution	1.1685	0.0066 \pm 0.0001	1.1458	169.4907 \pm 0.5148	1.1457	2.5564 \pm 0.0123
Cauchy Distribution	1.9013	0.0057 \pm 0.0000	1.6341	109.2575 \pm 0.1122	1.6340	3.8239 \pm 0.0166
Pareto Distribution	0.8399	0.0056 \pm 0.0000	0.8235	64.6855 \pm 0.0367	0.8235	2.1945 \pm 0.0138

Table E16 The table shows the length of the estimated geodesics for different methods on a CPU. The methods have been stopped if the norm of the gradient was less than 10^{-4} or if a maximum of 1,000 iterations has been reached. When the computational time was longer than 24 hours, the value is set to —.

Riemannian Manifold	trust-ncg (T=100)		trust-exact (T=100)	
	Length	Runtime Length	Runtime	
\mathbb{S}^2	2.2742	237.8402 ± 3.6964	2.2742	3.8066 ± 0.0204
\mathbb{S}^3	2.4342	340.5377 ± 1.5571	2.4342	6.8560 ± 0.0218
\mathbb{S}^5	2.3754	833.7228 ± 9.9481	2.3754	12.4160 ± 0.0325
\mathbb{S}^{10}	1.9521	9097.0312 ± 53.0355	1.9523	65.4820 ± 0.4559
\mathbb{S}^{20}	—	—	1.4816	424.0417 ± 1.6674
\mathbb{S}^{50}	—	—	—	—
\mathbb{S}^{100}	—	—	—	—
\mathbb{S}^{250}	—	—	—	—
\mathbb{S}^{500}	—	—	—	—
\mathbb{S}^{1000}	—	—	—	—
E (2)	1.9595	265.0164 ± 3.4124	1.9595	3.8934 ± 0.0312
E (3)	2.0499	726.9606 ± 6.6789	2.0498	4.7604 ± 0.1015
E (5)	1.8394	3843.9355 ± 39.4764	1.8393	16.1207 ± 0.2033
E (10)	—	—	1.5091	73.9657 ± 0.1229
E (20)	—	—	1.1718	398.0183 ± 1.7858
E (50)	—	—	—	—
E (100)	—	—	—	—
E (250)	—	—	—	—
E (500)	—	—	—	—
E (1000)	—	—	—	—
\mathbb{T}^2	9.9851	374.0822 ± 5.9408	9.9851	6.7989 ± 0.0304
\mathbb{H}^2	1.2498	627.2646 ± 7.3623	1.2498	5.0876 ± 0.0134
\mathcal{P} (2)	1.0669	594.2135 ± 5.1381	1.0669	4.0894 ± 0.0212
\mathcal{P} (3)	2.2639	2158.6843 ± 25.1696	2.2639	13.2320 ± 0.0803
Gaussian Distribution	2.5952	202.1364 ± 4.9068	2.5952	3.0117 ± 0.0225
Fréchet Distribution	1.1539	286.7279 ± 9.4552	1.1539	2.6002 ± 0.0147
Cauchy Distribution	1.6452	201.4917 ± 0.1496	1.6452	3.9414 ± 0.0098
Pareto Distribution	0.8297	233.9446 ± 0.2961	0.8297	2.3762 ± 0.0172

Table E17 The table shows the length of the estimated geodesics for different methods on a CPU. The methods have been stopped if the norm of the gradient was less than 10^{-4} or if a maximum of 1,000 iterations has been reached. When the computational time was longer than 24 hours, the value is set to —.

Riemannian Manifold	trust-neg ($T=50$)		trust-exact ($T=50$)	
	Length	Runtime	Length	Runtime
S^2	2.2478	115.7323 ± 1.0615	2.2478	3.6180 ± 0.0205
S^3	2.4064	138.8976 ± 0.8824	2.4064	4.6065 ± 0.0202
S^5	2.3480	272.6404 ± 1.2856	2.3480	7.6100 ± 0.0293
S^{10}	1.9274	1127.8496 ± 3.9055	1.9275	19.4117 ± 0.0371
S^{20}	1.4608	8353.8154 ± 153.6381	1.4610	110.3418 ± 0.4293
S^{50}	—	—	—	—
S^{100}	—	—	—	—
S^{250}	—	—	—	—
S^{500}	—	—	—	—
S^{1000}	—	—	—	—
E (2)	1.9330	101.3354 ± 0.2792	1.9330	3.8779 ± 0.0182
E (3)	2.0233	256.4745 ± 4.0010	2.0233	4.6605 ± 0.0146
E (5)	1.8046	1220.0194 ± 7.2318	1.8046	10.3930 ± 0.0328
E (10)	1.4753	3603.1384 ± 81.3956	1.4751	23.5777 ± 0.0401
E (20)	—	—	1.1434	109.4113 ± 0.0144
E (50)	—	—	—	—
E (100)	—	—	—	—
E (250)	—	—	—	—
E (500)	—	—	—	—
E (1000)	—	—	—	—
T^2	9.8955	189.0475 ± 0.1325	9.8955	7.5805 ± 0.0152
\mathbb{H}^2	1.2434	200.3231 ± 0.3463	1.2434	3.6404 ± 0.0076
\mathcal{P} (2)	1.0567	153.1577 ± 0.7454	1.0567	3.6134 ± 0.0305
\mathcal{P} (3)	2.2304	612.8415 ± 8.6455	2.2304	6.2574 ± 0.0139
Gaussian Distribution	2.5778	122.4479 ± 0.1045	2.5778	2.8004 ± 0.0155
Fréchet Distribution	1.1457	215.6763 ± 0.4161	1.1457	2.5323 ± 0.0123
Cauchy Distribution	1.6340	113.7271 ± 0.0720	1.6340	3.6122 ± 0.0207
Pareto Distribution	0.8235	80.3471 ± 0.8322	0.8235	2.2065 ± 0.0180

Table E18 The table shows the length of the estimated geodesics for different methods on a CPU. The methods have been stopped if the norm of the gradient was less than 10^{-4} or if a maximum of 1,000 iterations has been reached. When the computational time was longer than 24 hours, the value is set to —.

Riemannian Manifold	Sparse Newton (T=100)		Sparse Regularized Newton (T=100)	
	Length	Runtime Length	Runtime	Runtime
\mathbb{S}^2	2.2742	0.0180 ± 0.0002	2.2742	0.1017 ± 0.0017
\mathbb{S}^3	2.4342	0.0837 ± 0.0157	2.4342	0.3089 ± 0.0428
\mathbb{S}^5	2.3755	0.6723 ± 0.0409	2.3756	1.2203 ± 0.0887
\mathbb{S}^{10}	1.9449	256.4748 ± 20.0998	1.9531	4.3786 ± 0.3614
\mathbb{S}^{20}	1.7069	1130.3478 ± 127.1948	1.4943	20.3206 ± 1.5336
\mathbb{S}^{50}	1.0815	16216.8467 ± 2136.6802	1.0106	330.6598 ± 26.1208
\mathbb{S}^{100}	0.7522	1041.2721 ± 89.4723	0.7781	2863.6448 ± 233.2495
\mathbb{S}^{250}	0.4958	17070.7520 ± 2024.9161	—	—
\mathbb{S}^{500}	—	—	—	—
\mathbb{S}^{1000}	—	—	—	—
E (2)	1.9595	0.0254 ± 0.0002	1.9596	0.0915 ± 0.0028
E (3)	2.0498	0.1217 ± 0.0219	2.0499	0.3029 ± 0.0288
E (5)	1.8392	0.6774 ± 0.0721	1.8397	1.3500 ± 0.1241
E (10)	1.5247	300.2892 ± 23.3273	1.5114	4.4472 ± 0.3697
E (20)	1.4595	1101.5878 ± 115.0272	1.1961	17.6133 ± 1.2503
E (50)	0.8825	15145.3818 ± 1401.9972	0.8279	300.5634 ± 20.9595
E (100)	0.5922	839.4538 ± 68.5559	0.6402	2509.0547 ± 213.2646
E (250)	0.3919	16334.5381 ± 1370.7971	—	—
E (500)	—	—	—	—
E (1000)	—	—	—	—
\mathbb{T}^2	9.9851	0.0308 ± 0.0002	9.9851	0.0725 ± 0.0014
\mathbb{H}^2	1.2498	0.0225 ± 0.0004	1.2498	0.0948 ± 0.0036
\mathcal{P} (2)	1.0669	0.0692 ± 0.0182	1.0669	0.2395 ± 0.0334
\mathcal{P} (3)	2.3954	81.4573 ± 5.9683	2.2639	0.9140 ± 0.0747
Gaussian Distribution	2.5952	0.0123 ± 0.0001	2.5952	0.0472 ± 0.0007
Fréchet Distribution	1.1539	0.0085 ± 0.0001	1.1539	0.0500 ± 0.0004
Cauchy Distribution	1.6453	0.0120 ± 0.0001	1.6453	0.0519 ± 0.0002
Pareto Distribution	0.8297	0.0087 ± 0.0001	0.8297	0.0444 ± 0.0005

Table E19 The table shows the length of the estimated geodesics for different methods on a CPU. The methods have been stopped if the norm of the gradient was less than 10^{-4} or if a maximum of 1,000 iterations has been reached. When the computational time was longer than 24 hours, the value is set to —.

Riemannian Manifold	Sparse Newton ($T=50$)		Sparse Regularized Newton ($T=50$)	
	Length	Runtime	Length	Runtime
S^2	2.2478	0.0145 \pm 0.0001	2.2478	0.0500 \pm 0.0001
S^3	2.4064	0.0581 \pm 0.0177	2.4064	0.1629 \pm 0.0247
S^5	2.3480	0.2479 \pm 0.0150	2.3480	0.5728 \pm 0.0373
S^{10}	1.9274	2.2659 \pm 0.1698	1.9277	1.9943 \pm 0.1543
S^{20}	1.4610	230.5914 \pm 17.8627	1.4629	9.6611 \pm 0.7412
S^{50}	0.9948	7394.6870 \pm 845.2023	0.9720	128.6652 \pm 12.2889
S^{100}	0.6922	712.1899 \pm 54.3496	0.7163	1410.9242 \pm 104.6961
S^{250}	0.4581	13080.0830 \pm 1387.7233	—	—
S^{500}	—	—	—	—
S^{1000}	—	—	—	—
$E(2)$	1.9330	0.0207 \pm 0.0002	1.9330	0.0467 \pm 0.0002
$E(3)$	2.0233	0.0713 \pm 0.0186	2.0233	0.1612 \pm 0.0257
$E(5)$	1.8046	0.5449 \pm 0.0668	1.8050	0.7055 \pm 0.0764
$E(10)$	0.9473	133.1282 \pm 9.1672	1.4766	2.2189 \pm 0.2136
$E(20)$	1.2745	591.8414 \pm 35.1453	1.1484	9.3243 \pm 1.2287
$E(50)$	0.5985	7950.0571 \pm 865.0385	0.7965	146.5869 \pm 7.8365
$E(100)$	0.5707	775.0126 \pm 53.9842	0.5863	1405.4775 \pm 100.2025
$E(250)$	0.3882	9355.2041 \pm 978.4170	—	—
$E(500)$	—	—	—	—
$E(1000)$	—	—	—	—
T^2	9.8943	3.4085 \pm 0.2846	9.8955	0.0322 \pm 0.0004
\mathbb{H}^2	1.2434	0.0115 \pm 0.0003	1.2435	0.0441 \pm 0.0015
$\mathcal{P}(2)$	1.0567	0.0351 \pm 0.0159	1.0567	0.1206 \pm 0.0212
$\mathcal{P}(3)$	2.3328	42.5019 \pm 3.4439	2.2304	0.3846 \pm 0.0256
Gaussian Distribution	2.5778	0.0060 \pm 0.0001	2.5778	0.0199 \pm 0.0003
Fréchet Distribution	1.1457	0.0045 \pm 0.0001	1.1457	0.0217 \pm 0.0002
Cauchy Distribution	1.6340	0.0079 \pm 0.0002	1.6340	0.0223 \pm 0.0004
Pareto Distribution	0.8235	0.0042 \pm 0.0001	0.8235	0.0212 \pm 0.0003

Table E20 The table shows the length of the estimated geodesics for different methods on a CPU. The methods have been stopped if the norm of the gradient was less than 10^{-4} or if a maximum of 1,000 iterations has been reached. When the computational time was longer than 24 hours, the value is set to —.

Finsler Manifold	BFGS (T=100)			ADAM (T=100)			GEORCE (T=100)		
	Length	Runtime	Length	Runtime	Length	Runtime	Length	Runtime	
S^2	1.6525	244.9129 ± 0.0680	1.6536	0.4967 ± 0.0007	1.6525	0.0194 ± 0.0009			
S^3	1.7433	277.8015 ± 0.5819	1.7456	0.7639 ± 0.0031	1.7432	0.0362 ± 0.0001			
S^5	1.7032	435.6987 ± 4.6022	1.7377	4.6711 ± 0.0047	1.7029	0.4556 ± 0.0021			
S^{10}	1.4151	812.2809 ± 13.5968	1.5174	9.7974 ± 0.0052	1.4109	0.7473 ± 0.0029			
S^{20}	1.0951	1446.0956 ± 4.8038	1.2018	18.3489 ± 0.0747	1.0760	1.2856 ± 0.0016			
S^{50}	0.8216	5992.7261 ± 56.5973	0.8128	146.4556 ± 0.9341	0.7285	8.4758 ± 0.0234			
S^{100}	—	—	0.6187	498.9705 ± 0.4032	0.2570	15.3786 ± 0.0092			
S^{250}	—	—	0.5195	1397.6732 ± 0.7793	0.1622	132.5889 ± 0.1106			
S^{500}	—	—	0.4850	1954.3231 ± 14.1107	0.1404	364.5326 ± 1.8222			
S^{1000}	—	—	0.3843	5982.0884 ± 204.1833	0.1140	1338.9869 ± 2.3954			
E (2)	1.3616	230.0809 ± 1.3967	1.3621	0.5310 ± 0.0025	1.3618	0.0130 ± 0.0002			
E (3)	1.4001	416.6281 ± 5.5354	1.4087	0.8183 ± 0.0026	1.4023	0.1081 ± 0.0001			
E (5)	1.2951	638.7185 ± 2.7818	1.3265	4.3802 ± 0.0039	1.2956	0.4554 ± 0.0014			
E (10)	1.0733	741.9274 ± 12.3382	1.1229	9.7899 ± 0.0117	1.0804	0.5815 ± 0.0022			
E (20)	0.8510	1820.3137 ± 4.0734	0.8980	19.4614 ± 0.0039	0.8121	1.0671 ± 0.0044			
E (50)	0.5981	11191.9424 ± 597.7002	0.6325	146.6409 ± 0.1668	0.2842	4.4377 ± 0.0451			
E (100)	—	—	0.4936	491.8223 ± 0.2346	0.2009	14.5367 ± 0.0092			
E (250)	—	—	0.4159	1475.5049 ± 4.1430	0.1287	125.4187 ± 0.0888			
E (500)	—	—	0.4142	1984.7845 ± 10.5689	0.0967	373.2816 ± 0.4227			
E (1000)	—	—	0.3444	5929.4438 ± 167.1873	0.0799	1211.8812 ± 0.2511			
\mathbb{T}^2	7.3890	449.4798 ± 10.3282	7.3585	0.3294 ± 0.0018	6.8067	0.1126 ± 0.0002			
\mathbb{H}^2	1.3340	384.3149 ± 0.3044	1.3360	0.2744 ± 0.0024	1.3337	0.0094 ± 0.0001			
\mathcal{P} (2)	0.7291	414.8355 ± 3.0837	0.7338	0.6368 ± 0.0026	0.7292	0.0222 ± 0.0001			
\mathcal{P} (3)	1.2856	536.6575 ± 0.9323	1.2980	5.2824 ± 0.0540	1.2856	0.2094 ± 0.0004			
Gaussian Distribution	1.6878	163.4399 ± 0.1859	1.6936	0.1145 ± 0.0001	1.6878	0.0047 ± 0.0001			
Fréchet Distribution	0.5408	123.8418 ± 0.0499	0.5406	0.0585 ± 0.0001	0.5405	0.0021 ± 0.0001			
Cauchy Distribution	1.1134	182.3980 ± 2.2559	1.1133	0.1105 ± 0.0007	1.1133	0.0067 ± 0.0002			
Pareto Distribution	0.3884	84.8186 ± 0.0832	0.3885	0.0235 ± 0.0007	0.3883	0.0020 ± 0.0001			

Table E21 The table shows the length of the estimated geodesics for different methods on a CPU. The methods have been stopped if the norm of the gradient was less than 10^{-4} or if a maximum of 1,000 iterations has been reached. When the computational time was longer than 24 hours, the value is set to —.

Finsler Manifold	BFGS (T=50)		ADAM (T=50)		GEORCE (T=50)	
	Length	Runtime	Length	Runtime	Length	Runtime
S^2	1.6385	143.8810 \pm 0.2377	1.6385	0.2635 \pm 0.0001	1.6385	0.0134 \pm 0.0004
S^3	1.7298	146.9142 \pm 1.0720	1.7298	0.3666 \pm 0.0157	1.7297	0.0245 \pm 0.0001
S^5	1.6869	268.8883 \pm 1.4754	1.6878	2.2747 \pm 0.0047	1.6868	0.3351 \pm 0.0003
S^{10}	1.3919	452.0089 \pm 2.1364	1.4013	4.5715 \pm 0.0023	1.3908	0.6533 \pm 0.0180
S^{20}	1.0636	726.7038 \pm 5.3951	1.0830	8.3452 \pm 0.0040	1.0560	1.4084 \pm 0.0021
S^{50}	0.7320	1616.3099 \pm 8.8835	0.7427	71.9378 \pm 0.0786	0.3492	2.2147 \pm 0.0047
S^{100}	0.5832	4253.1743 \pm 13.8589	0.5511	291.3856 \pm 2.1209	0.2639	7.4223 \pm 0.0056
S^{250}	—	—	0.4094	1241.9021 \pm 7.3069	0.1686	52.1050 \pm 0.0283
S^{500}	—	—	0.3531	2204.0300 \pm 1.4159	0.1193	239.8835 \pm 0.2815
S^{1000}	—	—	0.3269	3347.6938 \pm 44.0626	0.0828	958.4282 \pm 7.2917
E (2)	1.3459	146.3793 \pm 0.7961	1.3460	0.0436 \pm 0.0001	1.3461	0.0084 \pm 0.0002
E (3)	1.3826	220.9877 \pm 2.8045	1.3870	0.3788 \pm 0.0023	1.3826	0.0972 \pm 0.0002
E (5)	1.2756	333.3406 \pm 0.9750	1.2780	2.2999 \pm 0.0031	1.2757	0.3920 \pm 0.0009
E (10)	0.5551	1225.0781 \pm 1.1283	1.0666	4.8530 \pm 0.0046	1.0126	0.8426 \pm 0.0013
E (20)	0.7340	1834.0602 \pm 20.3805	0.8404	8.9581 \pm 0.0200	0.7946	0.9224 \pm 0.0015
E (50)	0.5735	1238.1737 \pm 3.1700	0.5797	67.3310 \pm 0.0869	—	—
E (100)	0.4369	6365.4741 \pm 34.9823	0.4342	221.8947 \pm 1.4868	0.2042	6.5394 \pm 0.0437
E (250)	—	—	0.3234	935.4907 \pm 5.1887	0.1365	51.8779 \pm 0.0096
E (500)	—	—	0.2862	1512.1372 \pm 0.9319	0.0940	174.0314 \pm 0.2612
E (1000)	—	—	0.2723	2488.8240 \pm 38.0558	0.0893	681.7435 \pm 0.2447
T^2	7.0791	598.7396 \pm 0.0929	7.1796	0.1417 \pm 0.0002	9.0475	2.1109 \pm 0.0035
\mathbb{H}^2	1.3317	189.9143 \pm 0.0787	1.3316	0.1403 \pm 0.0026	1.3316	0.0070 \pm 0.0001
\mathcal{P} (2)	0.7249	224.4045 \pm 0.4114	0.7249	0.2194 \pm 0.0025	0.7249	0.0153 \pm 0.0001
\mathcal{P} (3)	1.2707	306.2382 \pm 0.1092	1.2735	2.7082 \pm 0.0075	1.2707	0.1276 \pm 0.0014
Gaussian Distribution	1.6806	88.1351 \pm 0.1027	1.6811	0.0569 \pm 0.0001	1.6806	0.0033 \pm 0.0001
Fréchet Distribution	0.5371	71.0994 \pm 0.0709	0.5370	0.0095 \pm 0.0000	0.5370	0.0015 \pm 0.0001
Cauchy Distribution	1.1084	94.0708 \pm 0.0792	1.1085	0.0075 \pm 0.0001	1.1084	0.0051 \pm 0.0001
Pareto Distribution	0.3857	46.7253 \pm 0.2142	0.3857	0.0084 \pm 0.0000	0.3857	0.0011 \pm 0.0001

Table E22 The table shows the length of the estimated geodesics for different methods on a CPU. The methods have been stopped if the norm of the gradient was less than 10^{-4} or if a maximum of 1,000 iterations has been reached. When the computational time was longer than 24 hours, the value is set to —.

Finsler Manifold	SGD (T=100)		CG (T=100)		dogleg (T=100)	
	Length	Runtime	Length	Runtime	Length	Runtime
S^2	1.7321	0.5226 \pm 0.0033	1.6536	864.7791 \pm 2.1507	1.6525	14.6421 \pm 0.0605
S^3	1.9179	0.8067 \pm 0.0005	1.7453	976.1121 \pm 13.5118	1.9228	4.1058 \pm 0.0123
S^5	2.1622	4.3635 \pm 0.0015	1.7099	1326.8875 \pm 10.6284	2.1703	5.8463 \pm 0.0436
S^{10}	2.4132	8.9293 \pm 0.0051	1.4427	801.4553 \pm 1.2792	2.4298	18.1452 \pm 0.0392
S^{20}	2.4912	19.4868 \pm 0.0023	1.2646	397.4008 \pm 2.7750	2.5207	98.6398 \pm 0.1329
S^{50}	2.2856	155.1010 \pm 0.2023	0.9295	274.3937 \pm 7.9883	—	—
S^{100}	1.9542	619.2194 \pm 0.4311	1.0756	221.9957 \pm 0.5803	—	—
S^{250}	1.4363	5475.3242 \pm 1.4705	0.8813	304.5134 \pm 0.0238	—	—
S^{500}	—	—	1.0790	31.3454 \pm 0.0388	—	—
S^{1000}	—	—	0.7859	137.1001 \pm 0.4771	—	—
E (2)	1.3705	0.5219 \pm 0.0024	1.3620	401.8943 \pm 0.7424	1.3616	14.9190 \pm 0.0640
E (3)	1.4388	0.8083 \pm 0.0019	1.4147	621.6700 \pm 3.4375	1.4397	4.6115 \pm 0.0556
E (5)	1.5358	4.6840 \pm 0.0044	1.3355	1523.9905 \pm 19.2195	1.5373	5.7719 \pm 0.0192
E (10)	1.6639	9.7218 \pm 0.0077	1.0329	2475.9639 \pm 93.5344	1.6672	18.9040 \pm 0.6761
E (20)	1.7336	19.6573 \pm 0.0115	0.9341	552.4011 \pm 0.4176	1.7403	95.1917 \pm 0.7952
E (50)	1.6453	145.3531 \pm 0.3967	0.7045	573.5270 \pm 6.1649	—	—
E (100)	1.4396	616.7589 \pm 0.2897	0.7510	394.1170 \pm 2.5401	—	—
E (250)	1.0800	4937.1353 \pm 67.9600	0.6266	784.1846 \pm 4.4711	—	—
E (500)	—	—	0.8183	31.6893 \pm 0.0422	—	—
E (1000)	—	—	0.5997	152.4971 \pm 0.5062	—	—
\mathbb{T}^2	—	—	8.5402	198.5802 \pm 0.2435	9.1903	4.4851 \pm 0.0162
\mathbb{H}^2	1.4881	0.2459 \pm 0.0024	1.3515	2582.8269 \pm 190.4313	1.3338	24.6057 \pm 0.0985
\mathcal{P} (2)	0.7860	0.6287 \pm 0.0027	0.7321	1333.9152 \pm 50.5504	0.7291	17.3661 \pm 0.0366
\mathcal{P} (3)	1.3773	5.3062 \pm 0.0015	1.2912	920.9217 \pm 15.9820	1.2856	35.0991 \pm 0.0589
Gaussian Distribution	1.9173	0.1056 \pm 0.0002	1.6881	820.4708 \pm 1.3159	1.6878	15.1765 \pm 0.0966
Fréchet Distribution	0.5499	0.1143 \pm 0.0009	0.5414	302.1487 \pm 0.2635	0.5405	9.8568 \pm 0.0634
Cauchy Distribution	1.4099	0.1025 \pm 0.0010	1.1138	821.1280 \pm 0.8392	1.1133	17.1469 \pm 0.0529
Pareto Distribution	0.3951	0.1124 \pm 0.0002	0.3899	206.6691 \pm 0.1273	0.3884	5.9249 \pm 0.0319

Table E23 The table shows the length of the estimated geodesics for different methods on a CPU. The methods have been stopped if the norm of the gradient was less than 10^{-4} or if a maximum of 1,000 iterations has been reached. When the computational time was longer than 24 hours, the value is set to —.

Finsler Manifold	SGD (T=50)		CG (T=50)		dogleg (T=50)	
	Length	Runtime	Length	Runtime	Length	Runtime
S^2	1.7109	0.2588 ± 0.0008	1.6385	439.9231 ± 4.5034	1.6385	14.8097 ± 0.0251
S^3	1.8925	0.3882 ± 0.0126	1.7298	496.1117 ± 4.7323	1.9113	3.6687 ± 0.0188
S^5	2.1279	2.2943 ± 0.0029	1.6874	658.4536 ± 4.7574	2.1588	4.0045 ± 0.0993
S^{10}	2.3586	4.8071 ± 0.0036	1.3911	896.1763 ± 6.7043	2.4194	6.7420 ± 0.0149
S^{20}	2.4105	9.5867 ± 0.0165	1.1016	622.5931 ± 6.0175	2.5121	25.6215 ± 0.0523
S^{50}	2.1971	71.2637 ± 0.0976	0.9319	177.8937 ± 1.2493	—	—
S^{100}	1.8917	295.5522 ± 1.0715	0.6486	219.8582 ± 1.3192	—	—
S^{250}	1.4136	2760.2507 ± 17.1501	0.5816	333.5332 ± 1.1282	—	—
S^{500}	1.0691	11508.7256 ± 47.0186	0.6111	510.0441 ± 1.7312	—	—
S^{1000}	—	—	0.6762	565.0285 ± 2.4234	—	—
E (2)	1.3601	0.2615 ± 0.0002	1.3461	422.3503 ± 12.1072	1.3460	20.7184 ± 0.0617
E (3)	1.4291	0.4036 ± 0.0006	1.3897	1200.0380 ± 33.6871	1.4325	4.2812 ± 0.0319
E (5)	1.5254	2.1031 ± 0.0024	1.2803	993.6235 ± 15.9966	1.5310	4.2148 ± 0.0296
E (10)	1.6487	4.7998 ± 0.0110	0.5483	2210.6582 ± 37.5507	1.6615	6.6250 ± 0.0132
E (20)	1.7096	9.5709 ± 0.0027	0.8485	564.2457 ± 0.9527	1.7353	23.9862 ± 0.0349
E (50)	1.6121	73.0136 ± 0.0216	0.6313	344.0060 ± 1.0995	—	—
E (100)	1.4125	313.0101 ± 0.3825	0.4981	331.0117 ± 1.3895	—	—
E (250)	1.0688	2706.8379 ± 8.4708	0.5508	378.6086 ± 0.2978	—	—
E (500)	0.8132	11307.9814 ± 281.9052	0.5677	751.1521 ± 1.0706	—	—
E (1000)	—	—	0.5987	77.4691 ± 0.2770	—	—
\mathbb{T}^2	<i>in.f</i>	0.0490 ± 0.0001	8.1529	167.4743 ± 2.8798	9.0475	4.3053 ± 0.0156
\mathbb{H}^2	1.4850	0.1246 ± 0.0040	1.3320	2460.6926 ± 57.6646	1.3316	19.7572 ± 0.0371
\mathcal{P} (2)	0.7739	0.3208 ± 0.0030	0.7250	712.9343 ± 11.1547	0.7249	14.5680 ± 0.0587
\mathcal{P} (3)	1.3514	2.6554 ± 0.0101	1.2709	788.9128 ± 8.9808	1.2707	22.6905 ± 0.0425
Gaussian Distribution	1.8463	0.0519 ± 0.0001	1.6807	283.3971 ± 6.7184	1.6806	16.2727 ± 0.1111
Fréchet Distribution	0.5455	0.0596 ± 0.0001	0.5372	253.2346 ± 0.2384	0.5370	9.3157 ± 0.0269
Cauchy Distribution	1.3641	0.0522 ± 0.0001	1.1088	360.8286 ± 0.4404	1.1084	16.8439 ± 0.0398
Pareto Distribution	0.3919	0.0555 ± 0.0001	0.3857	142.1006 ± 0.0492	0.3856	7.9442 ± 0.0303

Table E24 The table shows the length of the estimated geodesics for different methods on a CPU. The methods have been stopped if the norm of the gradient was less than 10^{-4} or if a maximum of 1,000 iterations has been reached. When the computational time was longer than 24 hours, the value is set to —.

Finsler Manifold	trust-ncg (T=100)		trust-exact (T=100)	
	Length	Runtime Length	Runtime	Runtime
S^2	1.6525	1261.5378 ± 7.7825	1.6525	14.7265 ± 0.0327
S^3	1.7432	1994.5762 ± 20.6694	1.7432	20.4180 ± 0.0359
S^5	1.7027	5603.5640 ± 76.5314	1.7027	38.7189 ± 0.0167
S^{10}	—	—	1.4108	184.4648 ± 0.3001
S^{20}	—	—	1.0769	1087.9535 ± 2.3390
S^{50}	—	—	—	—
S^{100}	—	—	—	—
S^{250}	—	—	—	—
S^{500}	—	—	—	—
S^{1000}	—	—	—	—
E (2)	1.3616	1019.1379 ± 8.5157	1.3616	15.4908 ± 0.0374
E (3)	1.3997	4148.8574 ± 2.3006	1.3997	31.8261 ± 0.1322
E (5)	1.2950	5965.7002 ± 44.3871	1.2950	40.3707 ± 0.0405
E (10)	—	—	1.0318	249.5034 ± 0.2415
E (20)	—	—	0.8109	1033.4261 ± 3.7266
E (50)	—	—	—	—
E (100)	—	—	—	—
E (250)	—	—	—	—
E (500)	—	—	—	—
E (1000)	—	—	—	—
\mathbb{T}^2	8.9015	348.9266 ± 0.5435	9.1722	56.1951 ± 0.0567
\mathbb{H}^2	1.3338	3365.4121 ± 15.3287	1.3338	24.6266 ± 0.1178
\mathcal{P} (2)	0.7291	2314.0154 ± 22.6535	0.7291	16.6480 ± 0.0684
\mathcal{P} (3)	1.2856	3887.0437 ± 81.9548	1.2856	42.8468 ± 0.1088
Gaussian Distribution	1.6878	1176.3495 ± 4.4250	1.6878	13.9002 ± 0.0735
Fréchet Distribution	0.5405	1173.9244 ± 4.9721	0.5405	9.5119 ± 0.0199
Cauchy Distribution	1.1133	1425.5028 ± 8.3454	1.1133	14.6313 ± 0.0416
Pareto Distribution	0.3884	406.4951 ± 4.4740	0.3884	5.9478 ± 0.0531

Table E25 The table shows the length of the estimated geodesics for different methods on a CPU. The methods have been stopped if the norm of the gradient was less than 10^{-4} or if a maximum of 1,000 iterations has been reached. When the computational time was longer than 24 hours, the value is set to —.

Finsler Manifold	trust-ncg (T=50)		trust-exact (T=50)	
	Length	Runtime	Length	Runtime
S^2	1.6385	461.6090 ± 2.4283	1.6385	14.9718 ± 0.0477
S^3	1.7297	738.8096 ± 14.1991	1.7297	18.2119 ± 0.0850
S^5	1.6868	1845.5012 ± 28.1314	1.6868	27.8877 ± 0.0334
S^{10}	1.3881	11723.0781 ± 267.5437	1.3881	72.3786 ± 0.5046
S^{20}	—	—	1.0591	321.4109 ± 0.3724
S^{50}	—	—	—	—
S^{100}	—	—	—	—
S^{250}	—	—	—	—
S^{500}	—	—	—	—
S^{1000}	—	—	—	—
E (2)	1.3460	760.6122 ± 4.1086	1.3460	18.9955 ± 0.0502
E (3)	1.3825	1558.1522 ± 1.8558	1.3825	25.1379 ± 0.0384
E (5)	1.2756	1658.7789 ± 4.1942	1.2755	31.1768 ± 0.0425
E (10)	1.0112	15954.7256 ± 487.2155	1.0109	104.7452 ± 1.3478
E (20)	—	—	0.8000	371.1157 ± 2.4557
E (50)	—	—	—	—
E (100)	—	—	—	—
E (250)	—	—	—	—
E (500)	—	—	—	—
E (1000)	—	—	—	—
\mathbb{T}^2	8.4108	364.3664 ± 2.8448	—	—
\mathbb{H}^2	1.3316	1348.8287 ± 29.8787	1.3316	19.5780 ± 0.0558
\mathcal{P} (2)	0.7249	702.5833 ± 1.9384	0.7249	14.2773 ± 0.0611
\mathcal{P} (3)	1.2707	1289.7513 ± 26.6135	1.2707	20.2860 ± 0.0433
Gaussian Distribution	1.6806	586.1818 ± 0.5433	1.6806	13.2321 ± 0.0358
Fréchet Distribution	0.5370	458.0856 ± 0.2181	0.5370	9.8644 ± 0.0257
Cauchy Distribution	1.1084	584.2502 ± 1.5708	1.1084	13.5337 ± 0.0222
Pareto Distribution	0.3856	366.4953 ± 0.2211	0.3856	8.6113 ± 0.0271

Table E26 The table shows the length of the estimated geodesics for different methods on a CPU. The methods have been stopped if the norm of the gradient was less than 10^{-4} or if a maximum of 1,000 iterations has been reached. When the computational time was longer than 24 hours, the value is set to —.

Finsler Manifold	Sparse Newton (T=100)		Sparse Regularized Newton (T=100)	
	Length	Runtime Length	Runtime	Runtime
S^2	1.6525	0.0632 ± 0.0009	1.6525	0.4062 ± 0.0273
S^3	1.7432	0.3018 ± 0.0366	1.7433	1.0369 ± 0.0880
S^5	1.7027	11.3808 ± 0.8228	1.7028	3.5064 ± 0.3096
S^{10}	1.4092	121.2282 ± 12.4696	1.4166	11.3672 ± 0.8836
S^{20}	1.3030	2840.8333 ± 230.3178	1.0865	52.2612 ± 5.1479
S^{50}	—	—	0.7556	809.2408 ± 68.4436
S^{100}	0.6141	16876.4219 ± 1314.8346	0.5968	6984.5508 ± 566.5103
S^{250}	—	—	—	—
S^{500}	—	—	—	—
S^{1000}	—	—	—	—
E (2)	1.3616	0.0916 ± 0.0029	1.3619	0.3423 ± 0.0174
E (3)	1.3997	0.5216 ± 0.0511	1.3997	1.3200 ± 0.1149
E (5)	1.5359	195.1668 ± 21.6446	1.2952	3.7467 ± 0.3126
E (10)	1.2272	560.2833 ± 45.3723	1.0807	10.0806 ± 0.7869
E (20)	1.0210	2939.9907 ± 244.8212	0.8555	52.9693 ± 5.7635
E (50)	—	—	0.6211	733.2034 ± 60.1911
E (100)	—	—	0.5132	6657.5815 ± 538.6103
E (250)	—	—	—	—
E (500)	—	—	—	—
E (1000)	—	—	—	—
\mathbb{T}^2	9.1903	27.4443 ± 2.4951	9.1903	27.5325 ± 2.2826
\mathbb{H}^2	1.3338	0.0816 ± 0.0019	1.3340	0.3529 ± 0.0227
\mathcal{P} (2)	0.7291	0.1944 ± 0.0248	0.7291	0.7200 ± 0.0868
\mathcal{P} (3)	1.2856	0.8253 ± 0.0772	1.2857	2.7333 ± 0.2234
Gaussian Distribution	1.6878	0.0636 ± 0.0006	1.6878	0.2146 ± 0.0122
Fréchet Distribution	0.5405	0.0368 ± 0.0001	0.5411	0.1835 ± 0.0107
Cauchy Distribution	1.1133	0.0720 ± 0.0015	1.1133	0.2079 ± 0.0126
Pareto Distribution	0.3884	0.0159 ± 0.0002	0.3886	0.1791 ± 0.0097

Table E27 The table shows the length of the estimated geodesics for different methods on a CPU. The methods have been stopped if the norm of the gradient was less than 10^{-4} or if a maximum of 1,000 iterations has been reached. When the computational time was longer than 24 hours, the value is set to —.

Finsler Manifold	Sparse Newton ($T=50$)		Sparse Regularized Newton ($T=50$)	
	Length	Runtime	Length	Runtime
S^2	1.6385	0.0504 ± 0.0005	1.6385	0.1821 ± 0.0097
S^3	1.7297	0.1977 ± 0.0270	1.7297	0.4563 ± 0.0481
S^5	1.6868	0.8981 ± 0.0788	1.6868	1.7423 ± 0.1372
S^{10}	1.3354	332.2007 ± 26.8370	1.3881	6.2534 ± 0.5135
S^{20}	0.8588	1562.1842 ± 125.8776	1.0579	30.9976 ± 2.3280
S^{50}	—	—	0.7149	364.6181 ± 32.4896
S^{100}	—	—	0.5364	3463.5500 ± 274.5852
S^{250}	—	—	—	—
S^{500}	—	—	—	—
S^{1000}	—	—	—	—
E (2)	1.3460	0.0658 ± 0.0015	1.3461	0.1592 ± 0.0057
E (3)	1.3825	0.2757 ± 0.0323	1.3825	0.6126 ± 0.0610
E (5)	1.2756	0.8444 ± 0.0827	1.2756	1.6410 ± 0.1521
E (10)	1.0106	276.2837 ± 26.7637	1.0575	284.1870 ± 27.1057
E (20)	0.8571	1488.3325 ± 147.3422	0.7945	30.3454 ± 1.4186
E (50)	—	—	0.5718	384.6765 ± 30.0164
E (100)	—	—	0.4397	3289.7231 ± 270.1520
E (250)	—	—	—	—
E (500)	—	—	—	—
E (1000)	—	—	—	—
T^2	9.0475	14.0754 ± 1.0615	9.0475	14.1199 ± 1.0787
\mathbb{H}^2	1.3316	0.0443 ± 0.0002	1.3317	0.1778 ± 0.0101
\mathcal{P} (2)	0.7249	0.1060 ± 0.0219	0.7249	0.3272 ± 0.0354
\mathcal{P} (3)	1.2707	0.4780 ± 0.0503	1.2707	1.1371 ± 0.1027
Gaussian Distribution	1.6806	0.0348 ± 0.0003	1.6807	0.0914 ± 0.0039
Fréchet Distribution	0.5370	0.0194 ± 0.0004	0.5371	0.0880 ± 0.0009
Cauchy Distribution	1.1084	0.0411 ± 0.0002	1.1085	0.0975 ± 0.0039
Pareto Distribution	0.3856	0.0174 ± 0.0004	0.3857	0.0884 ± 0.0048

Table E28 The table shows the length of the estimated geodesics for different methods on a CPU. The methods have been stopped if the norm of the gradient was less than 10^{-4} or if a maximum of 1,000 iterations has been reached. When the computational time was longer than 24 hours, the value is set to —.